Universitat de Barcelona
Facultat de Física

Institut de Física d'Altes Energies
Quantum Computing Technology group

Karlsruher Institut für Technologie
Physikalisches Institut

CHARACTERIZATION OF NITRIDIZED ALUMINIUM FOR QUANTUM COMPUTING HARDWARE APPLICATIONS

Ariadna Gómez del Pulgar Martínez

Supervisor:
Dr. Pol Forn-Díaz

Co-supervisor:
Dr. Elia Bertoldo

Master's Degree in Quantum Science and Technologies - Academic year 2023/2024

Characterization of nitridized aluminium for quantum computing hardware applications

Ariadna Gómez del Pulgar Martínez

Supervised by: Pol Forn-Díaz, Elia Bertoldo

Quantum Computing Technology group, Institut de Física d'Altes Energies, 08193 Bellaterra
Physikalisches Institut, Karlsruher Institut für Technologie, 76131 Karlsruhe
25 August 2024

Aluminium nitride (AlN_x) has been exhaustively studied in the literature as an insulator displaying piezoelectricity. However, nitridized aluminium (NitrAl) in its metallic state has been recently identified to be a superconductor at low enough temperatures. NitrAl is of particular interest for superconducting quantum circuits due to showcasing great potential to achieve high kinetic inductance combined with low loss. In this project, NitrAl thin films have been fabricated in the regime of high kinetic inductance and characterized at cryogenic temperatures, completing in this way the investigation of its superconducting properties carried out by the IFAE QCT group. Furthermore, microwave resonators have been designed and analyzed to ascertain the actual value of the kinetic inductance of NitrAl and its changes with temperature.

Keywords: NitrAl, Quantum Computing Hardware, Thin Film Sputtering, Kinetic Inductance, Superconductors, Resonators.

Ariadna Gómez del Pulgar Martínez: agomezma50@alumnes.ub.edu

Acknowledgements

Firstly, I would like to thank my supervisors, Pol Forn-Díaz and Elia Bertoldo, for the opportunity to join IFAE once again, for their exceptionally thorough direction of this thesis and for their brilliant guidance through the inconveniences that experimental physics inevitably involves. I am also especially thankful to Alba Torras-Coloma and Luca Cozzolino, PhD students of the QCT group, for their huge involvement in this project and the teachings about 4-point probe measurements and cleanroom procedures, as well as the Italian lessons. Additionally, I would like to thank David López-Núñez, former PhD student of the QCT group, for the previous codes that were adapted for this thesis and for always volunteering to help with any issue that might come up related to them. I would also like to appreciate the contributions of Gemma Rius, researcher at CNM-IMB, for the fabrication of NitrAl samples previous to this thesis.

Additionally, I would like to acknowledge Prof. Dr. Wolfgang Wernsdorfer for the extraordinary opportunity to visit KIT to fabricate and measure NitrAl thin films. It has been a great honor to get to work in such a reference center for superconductors, where grAl was first studied, and it has taught me invaluable research skills. Most importantly, I am extremely grateful to Prof. Dr. Christoph Sürgers for the exhaustive supervision and follow-up of my work during my stay in Karlsruhe, as well as the enlightening conversations about thin film superconductors and critical fields (and the Euro football cup).

Apart from the QCT group, I am thankful to the IFAE Pixel group for their warm welcome to the laboratory. Lunches and afternoon beers with Juan, Niraj, Keerthana, Merlin, Quim, Gangan, Pablo and Loris have eased troubling days and made research far more enjoyable.

Last, but not least, I would also like to thank my family and friends, especially my mom, sister and aunt, for their unconditional support even though they are clueless about physics and academia, for always encouraging me to continue my education journey and for bearing with my bad mood during the most stressful times of the thesis writing process.

To my dad, who would be the proudest to see this thesis.

Contents

1 Introduction

Quantum computing is foreseen to lead to an unprecedented revolution in information processing and problem solving [A+11]. Superconducting qubits [K+19] are, currently, one of the most promising approaches to achieve quantum supremacy. In particular, devices with a high characteristic impedance, greater than the resistance quantum $R_Q = h/4e^2 = 6.5\ \mathrm{k}\Omega$, are of particular interest due to their capacity to improve the time during which quantum bits can maintain states and the accuracy with which they can complete operations. A standard method to increase impedance is by enhancing one of its distinct components: the kinetic inductance. This is typically done by employing arrays of hundreds of Josephson junctions [B+12], which are superconducting layers separated by an insulator barrier through which electrons can tunnel. These structures, however, are highly difficult to produce because of their intricate fabrication process. Thus, a more straightforward method would be desirable.

A possible solution is the usage of materials that naturally have a large kinetic inductance of the order tenths or hundreds of nanohenries per unit area (nH/□), also known as superinductors. Typical examples of such materials are disordered superconductors and, especially, granular superconductors. An illustrative case of those is granular aluminum (grAl) [Gru19], which consists of an AlO_x matrix filled with pure Al grains that connect to each other via Josephson tunneling. As of today, grAl has been extensively introduced in superconducting quantum circuits, which, as a result, have improved their coherence time and quality [G+19].

More recently, nitridized aluminium (NitrAl, in short), which is similar in concept to grAl but contains nitride instead of oxide, has been proven to be a superconductor [TC+24] with great potential to achieve high kinetic inductance. Moreover, nitridized superconductors, such as TiN [V+10] and NbN [F+23] have much higher quality than bare materials. Hence, it is of significant importance to pursue a complete and exhaustive analysis of NitrAl.

In this work, NitrAl thin films with a variety thicknesses and quantities of N_2 in the range where it is expected to have greater kinetic inductance will be fabricated and characterized in terms of resistivity, critical temperature, critical magnetic field, critical current and response to oxidation and thermal annealing. Kinetic inductance, coherence length and mean free path will be estimated from those measurements. Additionally, $\lambda/4$ CPW resonators will be designed with the purpose of experimentally determining the kinetic inductance of NitrAl, and previously measured resonators will be analysed to examine their performance. With the characterization performed in this thesis, we provide evidence of superinductance values in several of the NitrAl thin films studied.

This work is structured as follows. Section 2 contains a comprehensive theoretical background regarding superconductors and resonators, the two main objects of study of this thesis. Following that, the results obtained for NitrAl are presented in the successive Sections 3 and 4. Lastly, the most relevant aspects that have emerged from this study are summarized in Section 5.

2 Theoretical concepts

In this chapter we will first introduce several theoretical concepts regarding the thin superconducting films that will be used throughout the thesis (Section 2.1). Then, we will describe the type of devices used in the thesis to analyze our thin films: microwave resonators (Section 2.2).

2.1 Superconductors

This section has been written following principally [Tin04, OD91].

2.1.1 Resistivity of thin films

Before diving in the description of superconducting materials, we must introduce two concepts that will appear recurrently in this work: sheet resistance and resistivity.

The opposition of materials to the conduction of electrical current is described by its resistance, R. Nevertheless, for the inspection of thin films, a further concept is more adequate: sheet resistance, R_S, is more adequate. This magnitude corresponds to the resistance of a square of a film of uniform thickness. Its quantification is achieved by conducting 4-point probe measurements [M+15]. In this procedure, four electrical probes are placed in a symmetric squared (the so-called Van der Pauw method) or linear arrangement along the thin film, as Figure 40 shows. Two of the probes are used to induce an electrical current between them, and the remaining two probes are dedicated to the measurement of the resulting voltage. From the measured resistance, and if different probe configurations give the same resistance value, sheet resistance can be computed as

$$R_S = R\frac{\pi}{\ln(2)}.$$

Sheet resistance is related to a second variable to account for the conducting properties of materials: resistivity, ρ. It can be either defined in terms of R_S or R as

$$\rho = R_S \cdot t = R\frac{W \cdot t}{L},$$

where W is the width of the film, t stands for its thickness and L represents its length. Note that the product $W \cdot t$ corresponds to the cross-section, A of the sample.

Although bulk resistivity is known for being thickness-independent, this statement is not true for thin films. In this case, it has an inversely proportional dependence on thickness due to surface scattering, as the Fuchs-Sondheimer model predicts [Fuc38, Son52], and grain-boundary scattering, explained by the Mayadas-Shatzke model [MS70].

2.1.2 Kinetic inductance

Depending on their level of conductivity, materials can be separated into insulators, which do not allow for current flow, and conductors. In that second group, an exceptional category stands out: superconductors.

Superconductors are materials that have the capability to conduct electricity losslessly, meaning that their electric resistance and, as a consequence, their resistivity are null. Moreover, these materials expel magnetic flux; in other words, in their interior, $B = 0$. This phenomenon is known as Meissner effect. These properties root in the fact that, microscopically, electrons in superconductors exist on a bound state below the Fermi level. In that state, pairs of electrons are formed due to an attractive potential that compensates the kinetic energy in excess of E_F. That potential originates from elastic phonon-electron interactions. Moreover, the bound electrons exist in a collective ground state. Those pairs, which have total spin 0 and anti-parallel momentum, are known as Cooper pairs. The full description of this anomaly is given by BCS theory [B+57].

The movement of Cooper pairs also gives rise to an interesting magnitude: kinetic inductance, L_{kin}. Its origin is related to the kinetic energy of Cooper pairs having a certain inertia to change their velocity whenever a change of the external electric field that

accelerates the electrons takes place. Thus, it is a contribution to total inductance that generates in the movement of current carriers, and may be independent of device geometry for some types of superconductors. For thin films, it can be computed as [R+16]

$$L_{kin,\,\square} = \frac{0.18\hbar}{k_B}\frac{R_{S,\,n}}{T_c}, \tag{1}$$

where $\hbar$ and k_B are Planck's and Boltzmann constants, respectively, $R_{S,\,n}$ is the normal state (that is, $T = 300$ K) sheet resistance and T_c is the critical temperature of the superconductor, which will be now properly introduced.

2.1.3 Critical parameters

Superconductors display non-resistive behaviours only below a certain temperature, which is characteristic of each material. This parameter is known as critical temperature, T_c. It can be identified as a drop in resistance (or, equivalently, resistivity) to null values when the material is cooled down.

Below T_c, there are several mechanisms to annihilate superconductivity. For instance, this may occur when applying a sufficiently strong electric current. The intensity at which this happens is known as critical current, I_c. Furthermore, superconductivity can be destroyed when external magnetic fields are applied. The field intensity at which superconductivity disappears is known as the critical field, B_c.

The action of critical fields can take place in two different manners. This divides superconductors into two types. For type-I superconductors, superconductivity is sharply destroyed in a first order phase transition. The magnetic field at which this happens is referred to as B_c. Contrary to that, for type-II superconductors, which do not repel magnetic flux perfectly, a second-order phase transition is involved. In this phenomenon, magnetic field vortices (also known as Abrikosov vortices [Abr57]) appear in the form of a vortex lattice at a lower field B_{c1}. While the material remains superconducting outside the vortices, the vortex density and size become greater with increasing applied magnetic field. At a certain critical field B_{c2}, vortices start to overlap: Cooper pairs then break apart due to the kinetic energy of the supercurrent exceeding the superconductivity gap energy (that is, the energy gap that prevents thermal excitations in superconductors) and superconductivity disappears. This is known as the orbital limit of superconductivity.

Grinzburg-Landau theory [GL50], which depicts a better description of inhomogenous superconductors than BCS theory, shows that the magnetic critical field B_{c2} dependence on temperature is

$$B_{c2}(T) = \frac{\phi_0}{2\pi\xi_{\mathrm{GL}}^2(T)}, \tag{2}$$

where:

- ϕ_0 is the magnetic flux quantum, $\phi_0 = \frac{h}{2e} = 2.0678 \cdot 10^{-15}$ Wb.
- $\xi_{\mathrm{GL}}(T)$ is the Grinzburg-Landau characteristic or coherence length. It is defined as the characteristic exponent of the phenomenology displayed by superconductors. Its temperature dependence for $T \sim T_c$ is given by

$$\xi_{\mathrm{GL}}(T) = \frac{\xi_{\mathrm{GL}}(0)}{\sqrt{1 - \frac{T}{T_c}}}. \tag{3}$$

By substituting Equation 3 in Equation 2, we obtain

$$B_{c2}(T) = \frac{\phi_0}{2\pi\xi^2_{\mathrm{GL}}(0)}\left(1 - \frac{T}{T_c}\right).$$

This is a linear expression, whose slope is given by

$$\frac{d\left[B_{c2}(T)\right]}{dT} \equiv \alpha = -\frac{\phi_0}{2\pi T_C \xi^2_{\mathrm{GL}}(0)} \Longrightarrow \xi_{\mathrm{GL}}(0) = \sqrt{-\frac{\phi_0}{2\pi T_c \alpha}}. \tag{4}$$

Disordered superconductors, such as NitrAl, belong to the dirty limit of superconductivity rather than the clean limit, where pure bulk Al lies within. In the dirty limit, the coherence length is modified as

$$\xi_{\mathrm{GL}}(T) = 0.855\sqrt{\frac{\xi_{\mathrm{BCS}}\ell}{1-\frac{T}{T_c}}} \Longrightarrow \xi_{\mathrm{GL}}(0) = 0.855\sqrt{\xi_{\mathrm{BCS}}\ell} \Longrightarrow \ell = \frac{1}{\xi_{\mathrm{BCS}}}\left[\frac{\xi_{\mathrm{GL}}(0)}{0.855}\right]^2. \tag{5}$$

In this expression, ξ_{BCS} corresponds to the coherence length given by BCS theory. Contrary to $\xi_{\mathrm{GL}}(T)$, ξ_{BCS} is a temperature-independent constant. Secondly, and most importantly, the mean free path, ℓ, is defined as the average distance that an electron can travel inside a superconductor before modifying its trajectory due to various scattering mechanisms.

There exists, additionally, a second mechanism for Cooper pair breaking when external magnetic fields are applied to type-II superconductors: they can also break due to the Zeeman splitting energy of electronic spin exceeding the superconducting gap energy, $\mu_{\mathrm{eff}}B > k_B T_c$, where μ_{eff} is the effective magnetic moment of the Cooper pair. This is known as Pauli-limited or Pauli paramagnetic effect [MT64]. Contrary to the orbital limit effect, this limit induces a first order transition, which, moreover, happens at much higher magnetic fields. Its temperature dependence, however, is more intricate, and sometimes material-dependent.

Due to studying thin films, which can even sometimes be approximated as 2D superconductors, the direction of the application of the external magnetic field with respect to the samples plays a fundamental role to which one of the two effects will dominate. External fields can be applied "perpendicularly" or "in parallel" to the surface vector. A comprehensive representation of the different fields is depicted in Figure 19. For perpendicular fields, the orbital limit effect will be reached before the Pauli limit has any impact. Hence, as explained before, the B_{c2} dependence on T is linear and the necessary magnetic fields to annihilate superconductivity are lower. On the other hand, for parallel fields, the orbital limit critical field is much higher than the Pauli limit critical field, since the effective area for vortices to appear is much smaller, and thus the latter will prevail. This can be identified as a larger critical field and a non-linear dependence of B_{c2} with T. Moreover, note that perpendicular fields allow for greater mean free paths, while for parallel fields they are restrained by the sample's thickness.

2.2 Microwave resonators

Having introduced the properties of superconductors that are of interest for this thesis, we will present the instruments that will allow for experimental kinetic inductance determination: resonators. This section has been mainly written following [Poz11].

Mechanical esonators are physical systems that, when exposed to vibrations, oscillate with greater amplitude at a certain frequency, called resonant frequency. In our case, the oscillations that will provoke resonance will be electromagnetic waves.

There exist two types of resonating devices depending on their relative size. On the one hand, if the dimensions of all the elements of the circuit are much smaller than the employed wavelength, then we are dealing with lumped-element circuits. In this case, voltage and current do not vary over the length of the circuit. On the other hand, distributed-parameter elements have a size comparable to the wavelength, and thus voltage and current may shift over the circuit. An example of lumped-element circuits are RLC resonators, and the most illustrative case of distributed-parameter elements are transmission lines.

RLC lumped-element resonators are electrical circuits assembled by the association of a resistor, R (which most of the times is simply a hypothetical element to account for the losses of the conductors of the circuit), an inductor, L, and a capacitor, C. These three building pieces can be arranged in a variety of topologies, giving rise to a diverse family of circuits. The most emblematic of them are the series and the parallel configuration.

As its name suggests, the parallel RLC resonator consists on the parallel association of a resistance, an inductor and a capacitor (see Figure 61). For this type of device, resonance occurs when the average electric energy stored in the capacitor equals the average magnetic energy stored in the inductor. Then, the input impedance (that is, the complex ratio of voltage to alternating current) is purely real, equal to R and maximum. This conjunction of phenomena occurs at the resonant frequency

$$\omega_0 = \frac{1}{\sqrt{LC}}.$$

On the other hand, the most commonly employed distributed element resonators are $\lambda/2$ and $\lambda/4$ transmission lines. The latter will be used during this thesis, and therefore we will concentrate on those.

Transmission lines are sections of cables through which electromagnetic waves travel. As per their physical implementation, there exist several approaches: microstrip lines, striplines, slotlines... However, one of the most preferred because of the easiness of their photolithography process and the high quality of the resulting devices are coplanar waveguides (CPW). These circuits consist on a central conducting line surrounded at each of its two sides by a wide, approximately semi-infinite conducting plane, which act as ground planes. The three conductors are all deposited on top of a dielectric substrate. Figure 62 shows a schematic representation of this assembly for better understanding.

As their name puts forward, $\lambda/4$ resonators [G+08] are transmission lines such that, at resonance, their length, l, is a quarter of a wavelength of the electromagnetic field:

$$l = \frac{\lambda}{4} + \frac{n\lambda}{2},\ n \in \mathbb{N} \cup \{0\}.$$

To impose this condition, $\lambda/4$ resonators are short-circuited in one end and open-circuited at the other end. The short-circuited end is terminated in a load impedance $Z_{\mathrm{L}} = 0$, where voltage is null and current is maximum. Contrary to this, the open-circuited termination has $Z_L = \infty$, and there current is null and voltage is maximum. Appendix I contains figures with examples of these type of transmission line resonators and their current distribution at resonance, showing a quarter of a wavelength.

Although being distributed-element devices, close to resonance this type of resonators can be thought of as lumped-element RLC parallel circuits. Thus, there exists an equivalence between their resonance frequencies by identifying

$$R = \frac{Z_0}{\alpha l},\quad L_n = \frac{2L_l l}{n^2\pi^2},\quad C = \frac{C_l l}{2},$$

where Z_0 is the characteristic impedance of the line (usually, $Z_0 = 50\ \Omega$), α is its attenuation constant, $n = 1, 2, 3, \ldots$ is the resonance mode number and L_l and C_l are the line's inductance and capacitance per unit length, respectively. While C_l depends on the geometry of the line and its effective permittivity, ε_{eff}, L_l sums up both geometric and kinetic inductance. Because of this last detail, by measuring the resonant frequency of $\lambda/4$ resonators, the kinetic inductance of a given material is attainable.

A method to identify and quantify the resonance of circuits are scattering parameters,

$$S_{ij} = \left.\frac{V_i^-}{V_j^+}\right|_{V_k^+=0 \text{ for } k\neq j}.$$

They are equivalently described by the scattering matrix, $[S]$, which, for two-port networks, has the form

$$\begin{pmatrix} V_1^- \\ V_2^- \end{pmatrix} = \begin{pmatrix} S_{11} & S_{12} \\ S_{21} & S_{22} \end{pmatrix} \begin{pmatrix} V_1^+ \\ V_2^+ \end{pmatrix}.$$

In this last two expressions, V is the amplitude of the voltage wave, the subindices $\{i,\ j\}$ stand for the input and output ports at which external power is driven to excite the resonators and the superindices $\{+,\ -\}$ represent incident and reflected waves, respectively. Thus, S_{ii} stand for the reflection of waves at each one of the input and output ports, while $S_{ij},\ i \neq j$, summarize the transmission between the two ports. As we will further comment later, resonance can be identified as dips or peaks in S parameters at the resonant frequency due to the maximizing of impedance.

The performance of resonators is reflected by their internal quality factor, Q_0. Q_0 is characteristic of the resonator itself and independent of any external elements. Resonating devices with a high Q_0 have small internal losses, and hence are good-performing.

A second quality factor can be defined so as to account for the losses caused by the external circuitry employed to measure the resonator and the coupling to it: the external quality factor, Q_e. The totality of the losses experienced by the resonator are enclosed by the loaded quality factor, Q_L. It is defined as 2π times the ratio of energy stored in the system to dissipated energy, and can be computed empirically from resonance S_{21} peaks and/or dips as $Q_L = \frac{\omega_0}{\Delta\omega}$, where $\Delta\omega = \omega_2 - \omega_1$ is the full width at half maximum amplitude at resonance.

The three different variables are related by

$$\frac{1}{Q_L} = \frac{1}{Q_0} + \frac{1}{Q_e}.$$

The coupling factor, g, further connects the different quality factors by

$$g = \frac{Q_0}{Q_e}.$$

If $g > 1$, then Q_0 dominates over Q_e; this is known as the overcoupled regime. Contrarily, if $g < 1$, Q_e becomes the main contribution to Q_L, establishing the undercoupled regime. The limit between this two behaviour regions, $g = 1$, corresponds to critical coupling.

Intrinsic losses in thin film superconductors may result from a variety of sources. At high temperature, the main contribution to losses corresponds to conduction losses. At the millikelvin range, however, two loss sources dominate over conduction: two-level systems (TLS) and quasiparticles (QP).

TLS [P+11] are a form of dielectric loss that arises from the resonant energy absorption by two-level defects existent in the surface, interface and bulk of insulators. Because of

this, they are especially dominant in nitrides and oxides. At temperatures below 1 K and low powers (near the single photon regime), TLS become the main loss source in superconductors. Thus, since that is the operating regime of superconducting qubits, TLS strongly constrict qubit coherence times. In that regime, the loss caused by these systems produces a shift in resonant frequency that can be modelled as

$$\Delta f_{\mathrm{TLS}} = \frac{1}{Q^0_{\mathrm{TLS}}} \frac{1}{\pi} \left\{ \mathrm{Re}\left[\Psi\left(\frac{1}{2} + \frac{hf_0}{2\pi i k_B T} \right) \right] - \ln\left(\frac{hf_0}{2\pi k_B T} \right) \right\}. \tag{6}$$

In this expression, Q^0_{TLS} is the quality factor due to TLS at low temperature and photon number and Ψ is the digamma function. The nature and origin of TLS, however, is still mostly undisclosed.

On the other hand, quasiparticles, or Bogoliubov quasiparticles, are excitations of Cooper pairs beyond their ground state. Thus, pairs break, originating a superposition of an electron and a hole. These defects also cause a shift in resonant frequency, which can be modelled as [S+20]

$$\Delta f_{\mathrm{QP}} = -\frac{1}{2} \alpha f_0 \frac{\Delta L_k}{L_k}, \tag{7}$$

where α is the ratio of kinetic inductance to total inductance and ΔL_k is the increase in kinetic inductance produced by the increase in the quasiparticle density. This last fact is particularly remarkable, as is an indicator of high kinetic inductance. Moreover, quasiparticles cause a certain dependence of Q_0 with temperature, which can be modelled as [B+11]

$$\frac{1}{Q_0} = \frac{\alpha}{\pi} \sqrt{\frac{2\Delta}{hf_0}} \frac{n_{\mathrm{QP}}(T)}{D(E_F)\Delta} + \frac{1}{Q_B}, \tag{8}$$

where Δ is the superconducting gap of the material, n_{QP} is the quasiparticle density, $D(E_F)$ is the density of states at the Fermi level and Q_B is the quality factor that reflects all other losses apart from quasiparticles. Hence, with increasing temperature, Q_0 is expected to diminish due to the increase in quasiparticle density. Equations 6 to 8 may be used to identify the different loss mechanisms in superconductors as a function of temperature, and thus can ascertain whether the resonator is dominated by QP or TLS loss.

3 NitrAl thin films

In this chapter, we will first describe the methods to fabricate thin films of NitrAl (Section 3.1). Then, in Section 3.2, we will characterize the thin films at cryogenic temperatures using the concepts introduced in Section 2. Finally, we will perform an analysis of the behaviour of thin films under thermal annealing and oxidation aimed at understanding their response during the fabrication process of a qubit device (Section 3.3).

3.1 Thin film fabrication

In order to study NitrAl thin films in the parameter regime of our interest, we fabricated a variety of samples with different quantities of nitrogen for thicknesses varying from 10 to 100 nm. The films will be later characterized at cryogenic temperatures in the following section.

The deposition of thin films executed for this thesis was performed at the facilities of KIT, and from now on we will refer to these samples as "2nd run". Additionally, several samples were already available as a result of a first study of NitrAl [TC+24] to address

their critical temperature, critical current and reaction to oxidation and thermal annealing. These prior samples had been fabricated externally at the facilities at the IMB-CNM (CSIC), in Bellaterra, and their measurement was performed at IFAE. We will refer to these former samples as "1st run".

All samples were fabricated via a sputtering process. In this procedure, charged ions are first bombarded onto a metal target source. Due to momentum exchange after the collision, metal atoms are then ejected from the source onto a substrate, leading to film deposition. Usually, the employed ions are noble gases, since they do not interact with other atomic species, thus avoiding undesired products. Appendix A contains a schematic representation of this process, as well as the exact fabrication parameters of each sample.

In our case, Ar ions originated from a plasma and an Al source were used during the sputtering process. Additionally, an N_2 gas flow was introduced so as to be incorporated in the resulting film, which is, then, AlN_x instead of pure Al. Since N_2 gas is not reactive, it is necessarily ionized into atomic N, wich does react with aluminium. The conditions to generate an argon plasma are ideal to simultaneously ionize N_2. The N_2 gas flow used in the sputtering process, ranging from 0.59 to 0.85 sccm, is the marker that we will use to infer the quantity of N_2 present in the different samples. By varying the N_2 flow, we are able to modify the resistivity of the resulting films, which can span from conducting to highly insulating. The Al source used was an RF gun, which is known to avoid charge build-up onto the substrate and requires the use of an impedance matcher to transform complex impedance into resistance to feed the RF power supply. The thickness of the produced samples was determined with a profilometer (model Ambios XP-2). As a substrate, highly resistive intrinsic Si wafers ($\rho \sim 10.000\ \Omega \cdot \text{cm}$) were used. This type of substrates are used in superconducting qubit devices, and so it is pertinent to use the same type to analyze the NitrAl thin films. Those were previously manually cut into $2{\times}2$ cm^2 or $2{\times}1$ cm^2 pieces with a diamond tip. Additionally, the substrate was cleaned following standard procedures with consecutive 5-minute-long dips in acetone and isopropanol in an ultrasonic bath and dried with an N_2 gas gun.

3.2 Thin film characterization

A complete characterization of the produced NitrAl thin films is perfored in this section. In particular, we will characterize their resistance, resistivity, critical temperature, critical field, critical current, mean free path, coherence length, kinetic inductance and response to oxidation and thermal annealing.

The samples of the 2nd run were measured at KIT with a Quantum Design Physical Property Measurement System dilution refrigerator. This apparatus can only reach temperatures above 1.8 K, which imposes a threshold in assessing the thin films' properties. On the other hand, the samples of the 1st run were measured at the IFAE installations with a BlueFors SD dilution refrigerator, which allows for cryogenic characterization down to 20 mK.

In order to perform the 4-point probe measurement of the 2nd run samples, we placed them onto an electrically insulated Cu sample holder. The wire bonds used to electrically contact the samples were applied directly on the samples' surface, following a linear configuration of the probes. A description of different wire-bonding methods is presented in Appendix C, alongside a discussion on them. On the other hand, the cryogenic 4-point probe measurement of the 1st run samples was completed by employing a PCB, which was later wire-bonded following a squared placement of the probes. A comprehensive image of this arrangement is also included in Appendix C. What is remarkable of this last method is that it allows for the easy switching of the current and voltage probes' placement, which

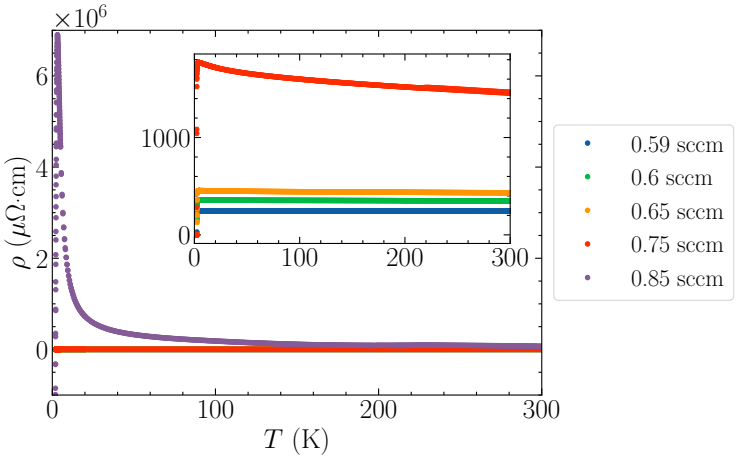

Figure 1: Resistivity of a selection 2nd run samples sputtered with different N_2 gas flows, all with a thickness of 100 nm. The inset shows a zoom-in of the resistivity in order to observe the response of the samples with lower N_2 gas flows during sputtering.

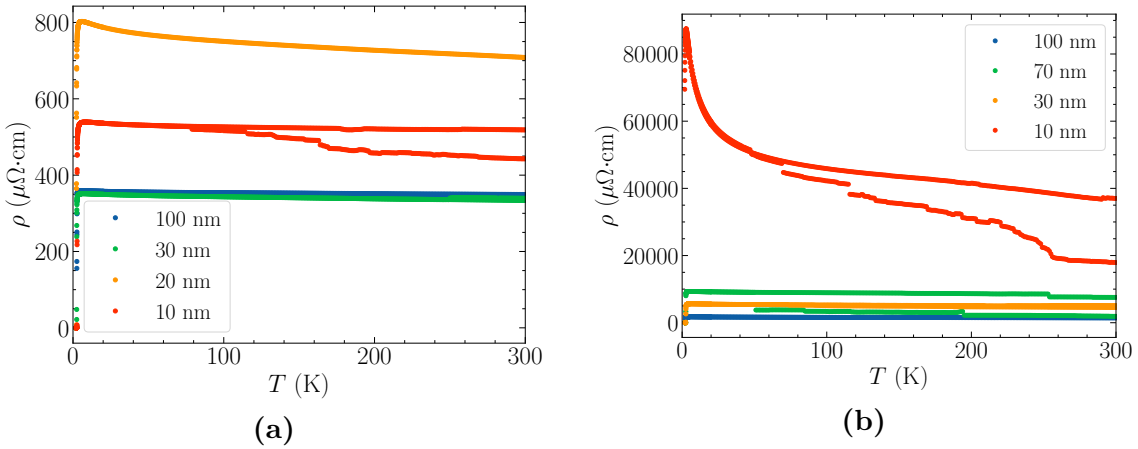

Figure 2: Resistivity of a selection of 2nd run samples of different thicknesses during cooldown and heatup. The cooldown values may have lower resistivity due to wire-bonding, as commented in Appendix C. **(a)** 0.6 sccm N_2 flow. **(b)** 0.75 sccm N_2 flow.

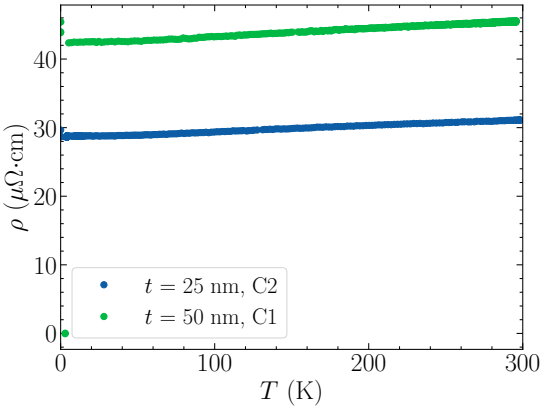

Figure 3: Resistivity of 1st run samples, sputtered with a 5% N_2/Ar gas flow ratio.

is translated into electrons flowing in different directions of the material. In our case, two different probe configurations were used, with one being rotated by 90° with respect to the other.

3.2.1 Temperature-dependent resistivity of thin films

First, we will review the samples from run 2. Figures 1 and 2 and Table 1 summarize obtained results regarding the resistivity of the NitrAl thin films fabricated in the 2nd run. Only a few of the measured samples were included in these illustrative images because of the curves for thicknesses between 100 to 30 nm being highly similar. The complete set of curves is shown in Appendix B. It is noteworthy that all of the obtained curves present an increase in resistivity before the metal-to-superconductor transition. This is a sign that, for all cases, we were close to the insulating regime rather than the conductor-like regime. Films in that range are expected to exhibit a larger kinetic inductance (see [TC+24]), and thus it is the regime of our interest.

In Figure 1 we find a consistent increase in resistivity with increasing N_2 flow during sputtering. This is in accordance with the fact that an increase in N_2 flow is translated into a larger quantity of nitrogen in the resulting NitrAl film, which then has a more disordered structure and consequently showcases a higher resistivity.

Conversely, the results of the 1st run samples are depicted in Figure 3 and Table 2. In this case, resistivity curves display a smoother transition, with no resistivity increases. This, alongside the smaller resistivity values, indicate that those samples are far from the metal-to-insulator transition.

Although, as mentioned in Section 2.1.1, an increase in resistivity was expected with decreasing thickness, this fact is not generally obvious, as Figures 2 and 3 show. Nevertheless, for the 2nd run samples, it is clear that samples of thicknesses between 10 and 20 nm, depending on the N_2 quantity of the films, present a much higher resistivity, as well as a more pronounced resistivity increase before the superconductor transition. Hence, the thin-film regime were resistivity strongly depends on thickness is reached for those thicknesses. Most importantly, this observations prove the fact that the insulator regime can be reached not only by increasing the N_2 flow during sputtering but also by decreasing the thickness.

Additionally, note that, for sample K ($t = 50$ nm), two different resistivity curves and critical temperature values were measured. Those results were obtained from the exact same sample measured twice within a week of difference, with 2 being the latest measurement. The shortness of this amount of time makes oxidation or aging a less likely cause of this phenomenon. A difference in resistivity is also noticed when measuring sample A* in different probe configurations. This dissimilarities might indicate the existence of different conducting paths for electrons inside the sample which are probed in different configurations, as would be common for disordered superconductors. The fact that no exceptional deviations in resistivity were observed when measuring sample B* in different probe configurations might hint that thicker samples, sputtered for a longer time, have a more ordered structure. This, however, should be corroborated with further XRD experiments, which are beyond of the scope of this thesis.

3.2.2 Critical temperature and kinetic inductance of thin films

From the resistivity curves for $T < 4$ K, T_c was ascertained by fitting a modified hyperbolic tangent of ρ vs. T. A thorough clarification of this method, as well as the raw data and the resulting fits, are included in Appendix D.

Tables 1 and 2 present the obtained critical temperature values. From those, alongside the normal state sheet resistance and the thickness of the films, also included in these tables, the kinetic inductance of the thin films was computed from Equation 1. Remarkably high L_{kin} values have been obtained, as intended.

A useful representation of critical temperature is that of Figure 4. A noticeable fact from this figure is the placement of the points, following the usual "dome" shape observed previously for NitrAl [TC+24] and grAl [LB+19]. The data observed here are located mostly to the right side of the dome. Furthermore, this representation allows for the discernment of samples with a potentially high kinetic inductance. Those, in comparison to other samples, usually showcase a higher resistivity and a lower critical temperature. Thus, in agreement with the kinetic inductance values from Equation 1, we can identify samples J, K, and L (blue, green and yellow stars in Figure 4, respectively), which were sputtered with a N_2 gas flow of 0.75 sccm and have thicknesses ranging from 30 to 70 nm, as strong candidates to being superinductors.

Note that, again, in Figure 4 a consistent trend within all samples of lower T_c for smaller thicknesses or higher N_2 gas flows during sputtering, as would be expected, is not observed. This may be the result of experimental inaccuracies during fabrication or the difficulty to acquire the desired characteristics due to disorder. Particularly, this would be reasonable in the samples produced during the first fabrication runs, when fabrication was still not fully calibrated.

Sample	**N_2 (sccm)**	**t (nm)**	**ρ_{RT} ($\mu\Omega$·cm)**	**$\rho_{4\,\text{K}}$ ($\mu\Omega$·cm)**	**T_c (K)**	**$L_{\text{kin},\square}$ (pH/□)**
A	0.59	100	248.050 ± 0.002	246.6982 ± 0.0004	2.4226 ± 0.0005	87.97 ± 0.02
B	0.6	100	349.321 ± 0.003	358.440 ± 0.001	2.713 ± 0.001	120.6 ± 0.1
C	0.6	70	∼ 460	461.142 ± 0.003	2.7152 ± 0.0005	209.58 ± 0.04
D	0.6	58	2654.55 ± 0.01	3943.570 ± 0.006	1.96 ± 0.01	2990 ± 20
E	0.6	30	339.391 ± 0.002	350.005 ± 0.009	2.552 ± 0.002	411.4 ± 0.3
F	0.6	20	708.364 ± 0.005	798.197 ± 0.003	2.316 ± 0.003	1488 ± 2
G	0.6	10	518.5326 ± 0.0006	531.003 ± 0.004	2.712 ± 0.002	1691 ± 1
H	0.65	100	431.675 ± 0.003	453.9440 ± 0.0004	2.567 ± 0.002	152.7 ± 0.1
I	0.75	100	1455.393 ± 0.004	1769.25 ± 0.03	2.209 ± 0.001	691.7 ± 0.4
J	0.75	70	∼ 8200	9269.04 ± 0.02	2.563 ± 0.001	4466 ± 2
K - 1	0.75	50	2318.87 ± 0.01	3019.293 ± 0.003	2.029 ± 0.006	2570 ± 7
K - 2	0.75	50	4745.73 ± 0.08	5769.34 ± 0.01	2.350 ± 0.005	4235 ± 8
L	0.75	30	5103.76 ± 0.02	5588.14 ± 0.04	2.562 ± 0.003	5456 ± 6
M	0.75	10	17904.4 ± 0.3	84076 ± 2	< 1.8	-
N	0.85	100	68880 ± 30	5988000 ± 2000	2.30 ± 0.01	(225 ± 1)·10^4

Table 1: Results of the 2nd run samples. The uncertainties in resistivity arise from the standard deviation of the linear regression of the $I-V$ measured curves, and the uncertainty in kinetic inductance was computed as $\delta L_{\text{kin},\square} = \frac{0.18h}{k_B \cdot t \cdot T_c}\sqrt{\delta\rho_{4\,\text{K}}^2 + \frac{\rho_{4\,\text{K}}^2}{T_c^2}\delta T_c^2}$.

Name	**t (nm)**	**ρ_{RT} ($\mu\Omega\cdot$cm)**	**$\rho_{4\,\text{K}}$ ($\mu\Omega\cdot$cm)**	**T_c (K)**	**$L_{\text{kin},\square}$ (pH/□)**	**I_c (mA)**
A⋆ - C1	25	46.58 ± 0.02	42.47 ± 0.02	3.033 ± 0.002	8.49 ± 0.05	1.936 ± 0.001
A⋆ - C2	25	31.08 ± 0.02	28.66 ± 0.03	3.002 ± 0.005	8.44 ± 0.05	1.320 ± 0.002
B⋆ - C1	50	45.48 ± 0.05	42.33 ± 0.01	3.2576 ± 0.0003	23.98 ± 0.05	0.44931 ± 5·10^{-5}
B⋆ - C2	50	44.65 ± 0.05	-	-	-	-

Table 2: Results of the 1st run samples, all sputtered with a 5% N_2/Ar gas flow ratio.

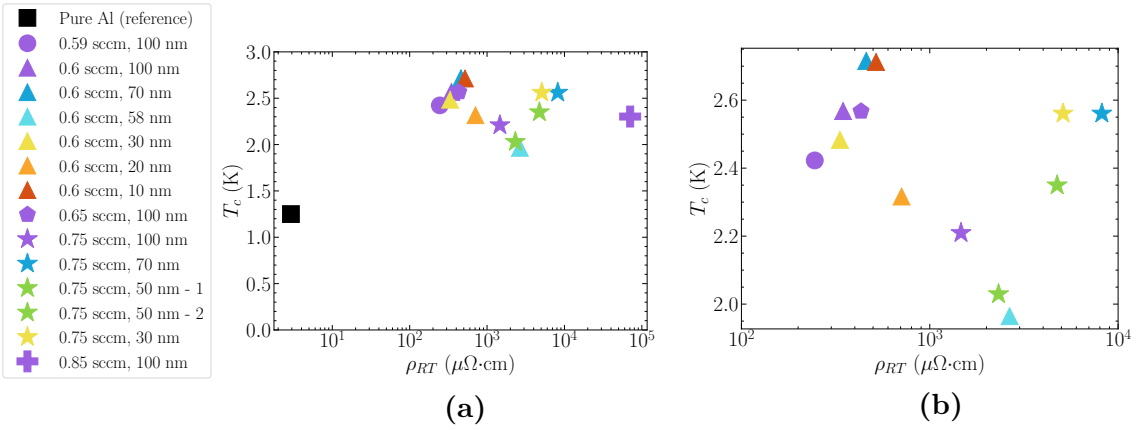

Figure 4: Critical temperature as a function of room temperature resistivity of the 2nd run samples. Same colors are used for different markers of different N_2 flow with the same thickness. The size of the markers used in this plot exceed the error bars found experimentally. **(a)** All samples, with the additional reference value of pure Al. **(b)** Zoom-in of samples with a more similar behaviour.

3.2.3 Critical field, coherence length and mean free path

A selection of the samples was further studied in terms of parallel and perpendicular critical magnetic fields. A discussion on how these measurements were carried out, alongside raw resistivity curves, can be found in Appendix E.

The perpendicular critical field dependencies on temperature are presented in Figure 5. As was expected from Grinzburg-Landau theory (see Section 2.1), perpendicular critical field demonstrates a linear dependence on temperature. Nonetheless, for small temperatures (or, equivalently, temperatures far from T_c), all curves start to differ from the linear relation, as was also predicted.

Oppositely, parallel critical field has a seemingly square-root dependence on temperature, as Figure 6 **(b)** exhibits. However, this relation gives the impression to become linear for $T \sim T_c$. As expected, the critical parallel field magnitudes necessary to break superconductivity are higher than in the perpendicular case. This confirms the difference in the involved

Name	**N_2 (sccm)**	**t (nm)**	**Slope (T/K)**	**$\xi_{GL}(0)$ (nm)**	**ℓ (nm)**
B	0.6	100	-0.64 ± 0.02	13.8 ± 0.2	0.162 ± 0.004
C	0.6	70	-0.621 ± 0.009	14.0 ± 0.1	0.167 ± 0.002
E	0.6	30	-0.902 ± 0.009	11.96 ± 0.06	0.122 ± 0.001
F	0.6	20	-1.83 ± 0.01	8.81 ± 0.03	0.0664 ± 0.0005
G	0.6	10	-0.78 ± 0.01	12.45 ± 0.09	0.133 ± 0.002
I	0.75	100	-2.25 ± 0.02	8.13 ± 0.04	0.0565 ± 0.0006
J	0.75	70	-1.19 ± 0.02	10.38 ± 0.07	0.092 ± 0.001
K - 1	0.75	50	-1.96 ± 0.06	9.1 ± 0.1	0.071 ± 0.002
L	0.75	30	-2.01 ± 0.03	7.99 ± 0.06	0.0457 ± 0.002

Table 3: Results of the application of external magnetic fields obtained for the different samples, alongside N_2 gas flow during sputtering and thickness. The slopes are those of the dependencies in Figure 5, and their uncertainties correspond to the standard deviation of the pertinent linear regressions. The uncertainties in $\xi_{GL}(0)$ and ℓ have been computed as $\delta\xi_{GL}(0) = \frac{1}{2}\sqrt{-\frac{\phi_0}{2\pi T_c \alpha^3}}\delta\alpha$ and $\delta\ell = \frac{2\xi_{GL}(0)}{\xi_{BCS}0.855^2}\delta\xi_{GL}(0)$.

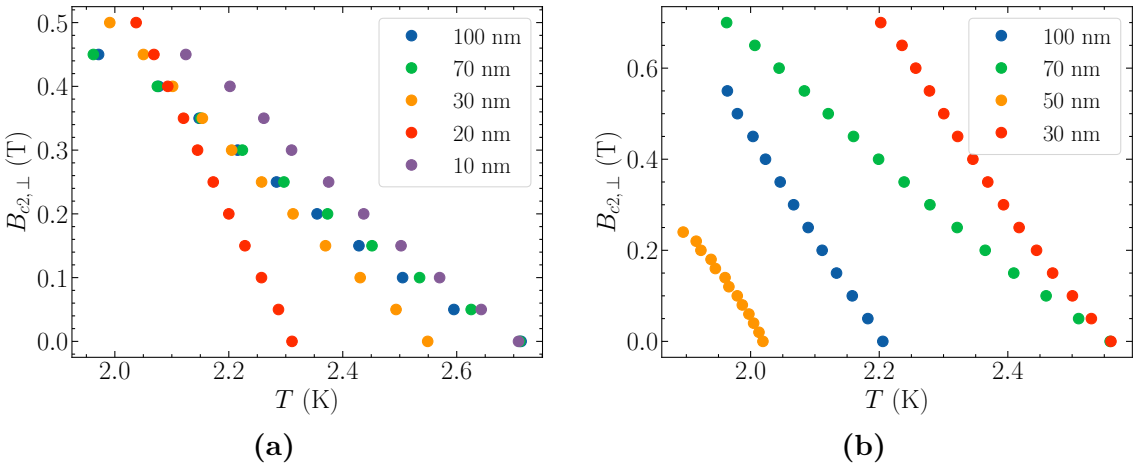

Figure 5: Perpendicular critical field as a function of temperature of 2nd run samples of different thicknesses. **(a)** 0.6 sccm N_2 flow. **(b)** 0.75 sccm N_2 flow.

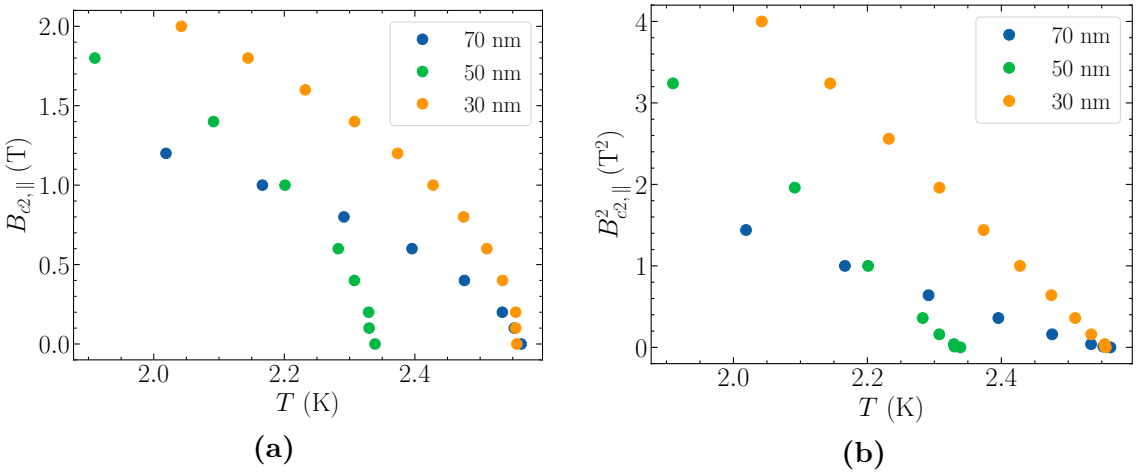

Figure 6: Parallel critical field as a function of temperature of 2nd run samples of different thicknesses sputtered with a N_2 gas flow of 0.75 sccm. **(a)** Critical field. **(b)** Squared critical field.

superconductivity limits and pair-breaking mechanisms when applying perpendicular and parallel external magnetic fields to NitrAl thin films, as well as the anisotropy of the material.

As explained in Section 2.1, from the slope of the dispersions in Figure 5 it is possible to compute the Grinzburg-Landau coherence length at $T = 0$ K by utilizing Equation 4. The slopes and resulting coherence lengths are included in Table 3. From this, it is notable that, generally, $\xi_{GL}(0)$ decreases with thickness. Moreover, its values are lower for the samples sputtered with a 0.75 sccm N_2 gas flow than for those fabricated with a 0.6 sccm N_2 gas flow. Both particularities are consistent with the fact that resistivity can be incremented either by increasing the N_2 flow or by decreasing the thickness of the sample. This increases disorder in the samples, which is translated into difficulties in the movement of electrons. Nonetheless, samples F, G, J and K, from which stemmed an anomalously high coherence length, do not follow the aforementioned thickness trend. This could be due to fabrication miscallibration of those samples, as statistical reproducibility of the different samples could not be performed due to the limited amount of time to carry out the fabrication and characterization of the thin films.

From $\xi_{GL}(0)$, we have been able to compute ℓ by means of Equation 5. In order to do so, we have used the value of ξ_{BCS} corresponding to pure Al, $\xi_{BCS} = 1600$ nm [OD91]. This approximation is based on the assumption that electrons travel, generally, through pure Al grains and the tunnelling through the nitrogen grains introduces no significant variations in ξ_{BCS}. The extraordinarily small results that have been obtained, also included in Table 3, show that electrons can only travel a minuscule distance before being scattered by nitrogen grains and their AlN_x layers, which is a sign of the high disorder of the samples. However, we made a strong assumption about using ξ_{BCS} of bulk aluminium, which shows a very large value compared to other type-I superconductors. It would be necessary here to produce NitrAl samples much thicker and estimate ξ_{BCS} of those for a proper characterization of ℓ. Despite this, the increase in mean free path with thickness and quantity of nitrogen suggests the decrease of disorder for thicker and less resistive samples.

3.2.4 Critical current

As mentioned in Section 2.1, superconductivity can also disappear by the application of sufficiently high electrical currents to the samples at temperatures below T_c. Samples A* and B*, from the 1st run, were assessed in terms of critical current to check its dependence on thickness. The raw data from which this results are derived are included in Appendix F.

The results obtained for these samples, presented in Table 2, show a rise in I_c with thickness. We can further complete this thickness study with the result in [TC+24]. In this work, for samples with a 5% N_2/Ar gas flow ratio during sputtering and a thickness of 100 nm, a critical current between 65 and 95 mA was measured. This reinforces the increase in I_c with thickness that was noticed during this thesis.

It is noteworthy that the obtained I_c are in agreement when applying positive and negative currents. What is more, even though there exists a difference in the measured resistivity values for sample A* depending on the configuration of the position of the probes, the obtained I_c are consistent in both configurations.

3.3 Oxidation and thermal annealing

As an approach to study how different fabrication procedures can affect the performance of NitrAl, an oxidation process and successive thermal annealing treatments were applied.

Thermal annealing is a process that aims to modify the surface morphology of materials by exposing thin films to a given temperature for a certain amount of time. This procedure is known to enhance the behavior of materials by liberating stress, controlling roughness and generally improving their structure. Previous studies performed on Au thin films [AM+13] have shown that the cause of this behavior might be a vertical growth of surface protrusions and a decrease of the grain size (that is, the base of the protrusion). This modification of the material grains is transitory up until a certain temperature, which is intrinsic of each material, and the protrusions recover their original form after a certain time. Past that characteristic temperature point, structural changes become permanent.

The following consecutive treatments of several NitrAl were applied:

- 16 hours of oxidation in standard temperature and pressure conditions. This simply consisted on exposing the samples to air, not stored in a dessicator in vacuum and low humidity.
- A bake of 2 hours at 100°C in standard pressure conditions.
- A second bake of 2 hours at 100°C in standard pressure conditions.

- A bake of 2 hours at 200°C in standard pressure conditions.

The bakes were performed in a hotplate under cleanroom conditions. After each individual bake, the samples were left for cooling in a dessicator for about three hours to prevent excessive surface damage. Following that, the measurement of the resistance of the films was done with an MPI Corporation probe station, a Keithley 2634B sourcemeter and the help of the software Labber, by Keysight. A lapse of one to two days was allowed between bakes so as to investigate whether changes in resistivity were permanent or transitory.

The samples selected were four thin films of the 1st run, all of them of thickness $t = 100$ nm and sputtered under similar conditions. Three of the films were sputtered with a 13.3% N_2/Ar gas flow ratio, while the fourth one was fabricated with a 15% ratio. From previous measurements [TC+24], the 13.3% films were known to not have reached the metal-to-insulator transition, but were highly resistive. The 15% film, on the other hand, was determined to be insulating. With the thermal annealing of this last sample, we aimed to address whether it is plausible to lower its resistivity down to the conducting regime. Moreover, for comparison purposes, several grAl and Al samples were also subjected to the thermal annealing processes. These samples, however, were not exposed to the oxidation step.

The evolution of the resistivity of the samples throughout the series of different manipulations is depicted in Figure 7, and the corresponding $I - V$ curves from which each point is computed by linear regression are presented in Appendix G.

In Figure 7 **(a)** it is reflected that all NitrAl thin films follow a comparable progression. An exceptional increase in resistivity was observed after the oxidation step, as was forecast due to the formation of an insulating layer at the surface of the films. This increase, however, was diminished with the first bake. Before and after the bakes, resistivity is reduced, as was expected, with a more pronounced drop for the third bake, which is in agreement with the usage of higher temperatures. The restoring of the resistivity figures in between bakes points out that the modifications of the films introduced by thermal annealing were temporary. The differences in the values of resistivity of the three individual samples might indicate the difficulty in reproducing thin film characteristics even when employing the same sputtering features, just as happens with grAl.

In Figure 7 **(b)**, it is notable that all grAl samples also pursue a similar evolution, despite their dissimilar resistivities. Nonetheless, the expected resistivity decrease after each bake is not always exhibited: it is only exceptionally clear after the 200°C bake. Restoration of resistivity levels to previous values in between bakes is also not clear, which might indicate that the temperature for which alterations caused by thermalization become irreversible is lower. Additionally, when measuring the samples in probe configurations rotated by 90° one with respect to the other after performing bakes, different results arise, pointing to anisotropy.

This two last particularities were also inferred for Al, as Figure 7 **(c)** reflects. These films showcase the lowest resistivity of all, as was expected due to the omission of dopants in the material. For Al, furthermore, it is particularly striking that, after a bake, resistivity always increases when placing the probes in one configuration and decreases when positioning them with a 90° rotation. The reason behind this may also be anisotropy, as for grAl, which is translated into variations in resistivity for different directions of the material. Another possible cause may be the crystal structure of Al, which, in some cases, is Al(111). This, however, must be confirmed with XRD experiments. Those were attempted for the KIT NitrAl 2nd run samples with no remarkable results, which, again, is a sign of the great disorder of the samples resulting from their high nitridation.

Additionally, the thickness variety in the Al films unveiled that resistivity increases

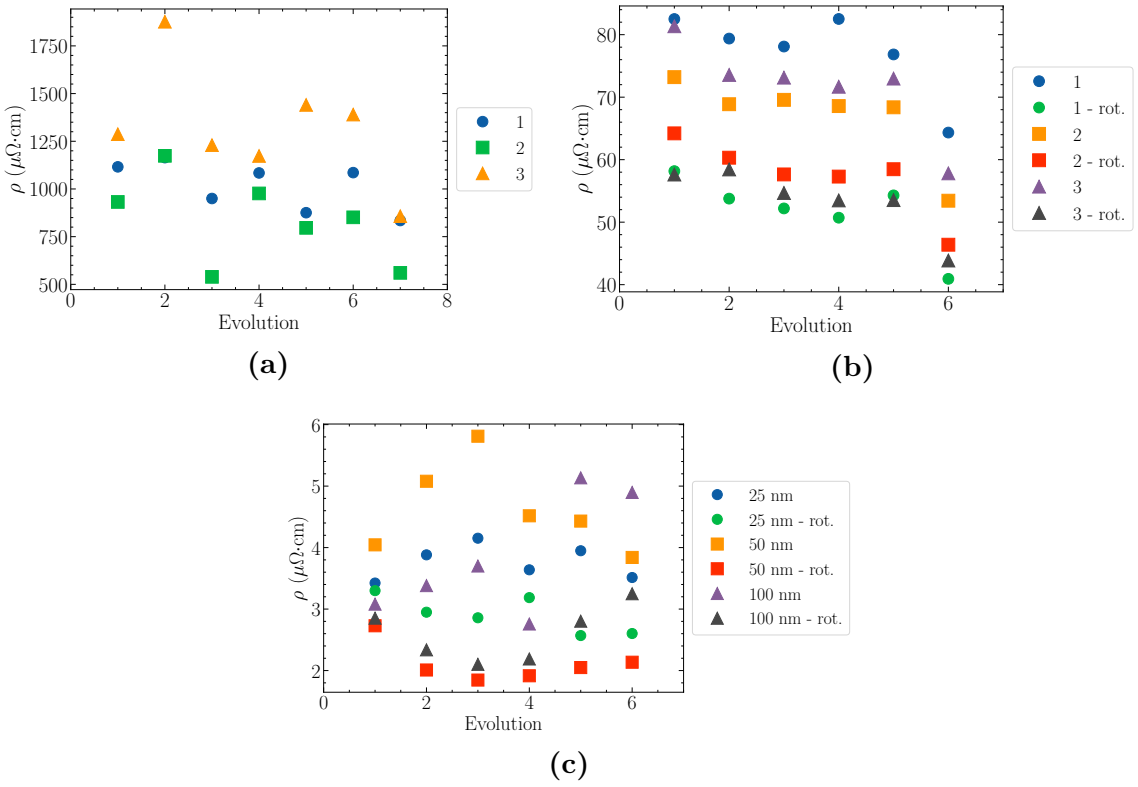

Figure 7: Evolution of resistivity with consecutive oxidation and/or thermal treatments. The x-axes represent the following chronologically events: 1. Measurement of unprocessed films. 2. After 16 h of oxidation, if applicable. 3. After first bake at 100 °C and 3 hours of cooling in vacuum. 4. Before second bake at 100°C. 5. After second bake at 100°C and 3 hours of cooling in vacuum. 6. Before bake at 200°C. 7. After bake at 200°C and 3 hours of cooling in vacuum. **(a)** NitrAl, sputtered with a 13.3% N_2/Ar gas flow ratio, with $t = 100$ nm. **(b)** grAl, with $t = 100$ nm. **(c)** Al.

with decreasing thickness also for that material. This is in agreement with the described predictions of Fuchs-Sondheimer theory for the inverse dependence of resistivity on thickness for thin films.

Concerning the 15% NitrAl studied thin film, it did not showcase any resistance modification for an insulator-to-metal transition. This can be inferred from its $I-V$ curves not resembling a linear fashion.

After this series of procedures, the NitrAl samples were spin-coated, and the three bakes were then repeated. This was done to address whether the changes in resistance observed in the previous treatments were due to the liberation of gas bubbles from within the samples, or, generally, if any observable modification of the surface of the samples was observable. The spin-coating of the films was accomplished by following standard procedures, which includes a bake at 80°C. Augmented images of the surface were taken with the help of a Leica optical microscope.

The obtained images of a representative 13.3% sample and the 15% sample are shown in Figures 8 and 57, respectively. The most outstanding feature of these images is the appearance of bubbles in the resist after the bake at 200°C (see **(c)**). All three 13.3% samples experienced this same phenomenon at this step, which, contrarily, did not happen to the 15% thin film. Recall that the main difference between those two types of samples is that the 13.3% samples are conducting, while the 15% sample shows an insulating

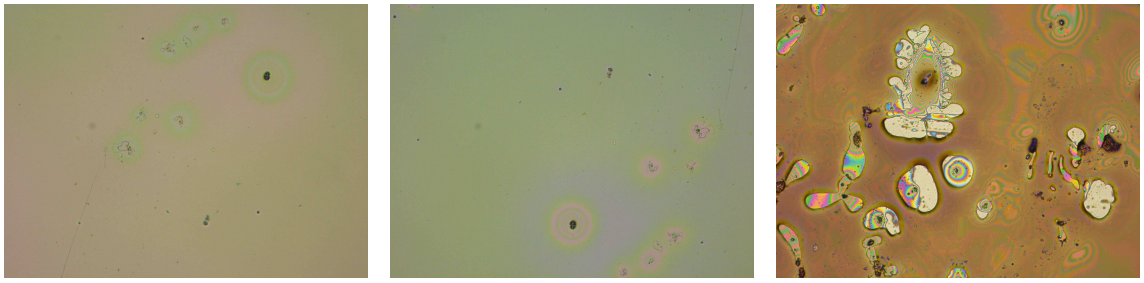

(a) **(b)** **(c)**

Figure 8: 20x augmented optical images of 1st run samples with resist sputtered with a 13.3% N_2/Ar gas flow ratio. **(a)** Before bakes. **(b)** After a 2-hour long bake at 100°C. **(c)** After a 2-hour long bake at 200°C.

behaviour. This rising of air bubbles for the conducting samples at 200°C may identify gas liberation as the cause of the sizable improvement in resistivity, which can lead to a possibly permanent modulation of the surface grain protrusions that was not acquired for lower temperatures.

4 Superconducting microwave resonators

Although strong evidence of the high kinetic inductance of NitrAl has been shown in Section 3, its exact value still remains unknown. In this section, we provide a direct estimate of the kinetic inductance of the NitrAl thin films employing superconducting microwave resonators.

4.1 Photolithographic mask design, simulation and fitting

Short-circuited quarter-wavelength distributed-element coplanar waveguide resonators, described in Section 2.2, will be utilized for the determination of NitrAl's L_{kin}. For this purpose, a photolithographic mask design previously developed in the IFAE QCT group was modified, simulated and fitted to meet a number of conditions.

The design contains five $\lambda/4$ CPW resonators of different lengths (and, consequently, different resonant frequencies) coupled to a feedline that delivers power to them. The coupling, in this case, is inductive, as the short-circuited end is located closer to the feedline. Images of the resonators and their distribution can be found in Appendix I.

The devices must adapt to a series of requirements to be measurable by the available equipment at IFAE and to facilitate the study of their most interesting attributes. Sonnet Software [son] was employed to simulate the different resonators as a means to check which design parameters met the required characteristics.

Firstly, their fundamental mode resonant frequency, f_0, must be at least 4.5 GHz and at most 8 GHz. The reason behind this is that, due to the presence of filters and circulators in the dilution refrigerator, only that frequency range is measurable, as it is common in setups employing superconducting qubits.

Secondly, the dips in the modulus of the S_{21} parameter indicating resonances should have a depth of at least -10 dB. This is needed because of the fact that it was previously shown in the laboratory that it is the minimum depth that can be detected by the Vector Network Analyzer that will be used for the measurement of the resonators.

Lastly, the devices should be critically coupled to the feedline: that is, the ratio of internal to external quality factor should be 1. This condition was chosen to be imposed so

Resonator	f_0 (GHz)	Q_0	Q_e	Q_L	g
1	4.69	22816.23	12231.30	8640.97	1.87
5	4.92	21827.57	11017.90	8172.78	1.98

Table 4: Simulated parameters for the resonators of lower and highest resonant frequencies.

as to better infer the internal quality factor of the resonators. Recall that this magnitude reflects the internal losses of the resonators regardless of external circuitry elements.

The geometry and materials that conformed the simulated resonators are detailed in Appendix I. For the meshing that conforms the subsections for the matrix filling and solving, a staircase meshing formed by 2×2 μm cells was implemented, since the smallest distance in the design was of 6 μm. The use of conformal meshing, despite being more accurate for rounded shapes, was discarded due to the vast increase in simulation time that it implied. Finally, adaptative frequency sweeps were run, with several consecutive refinements around the resonance dip. The simulations were performed at the Port d'Informació Científica (PIC) server in order to minimize the simulation time.

The resonance of the simulated devices was ascertained from their transmission S_{21} parameter, defined in Section 2.2. Since the input and output ports are placed at the ends of the feedline that delivers power into the resonators, it is the feedline's transmission which is, indeed, studied. Recall that the input impedance of $\lambda/4$ resonators is maximum at resonance. Consequently, the power leakage from the feedline to the resonators will be higher at that point. Because of that, the feedline's transmission parameters will experience a minimum when resonance occurs [Doy08].

The modulus of the S_{21} parameter of the shortest and longest resonators as a function of frequency is presented in Figure 66 in Appendix I. Only those resonators are presented because the resonances of the remaining devices will lie within the boundaries set by the two shown in the figure. From the dips in $|S_{21}|$ at resonance, resonant frequency and quality factors were derived following the method contained in Appendix H. The corroboration of having obtained the fundamental resonance mode, and not other excited modes, was performed by checking the electrical current distribution, included in Appendix I. The parameters that were extracted from the simulations are included in Table 4.

From the simulations, the distance to the feedline that was chosen for the resonators as ideal to meet the requirements was $d = 14$ μm, and the five resonators were designed to have lengths $l = 2289.67$, 2325.46, 2343.76, 2362.36 and 2400.46 μm. The prerequisite $g = 1$, however, is not attained. This is due to the fact that the higher the distance to the feedline, the weakest it will sense the resonator, and consequently the resonance dip will be shallower and further from the -10 dB prerequisite. Thus, the distance from the resonators to the feedline had to be chosen to be as close as possible to the critical coupling while still obtaining measurable resonators. Furthermore, the internal quality factors that were obtained were quite low, potentially due to dielectric loss.

4.2 Resonator data analysis

To ascertain the kinetic inductance of several 1st run NitrAl films, a first set of resonators was sputtered and photolithographied at CNM and measured at low temperature at IFAE. Moreover, pure Al resonators were also simultaneously fabricated for comparison purposes. The measurements were performed with the aforementioned BlueFors SD dilution refrigerator and an E5071B Agilent Technologies VNA. The data analysis of those early

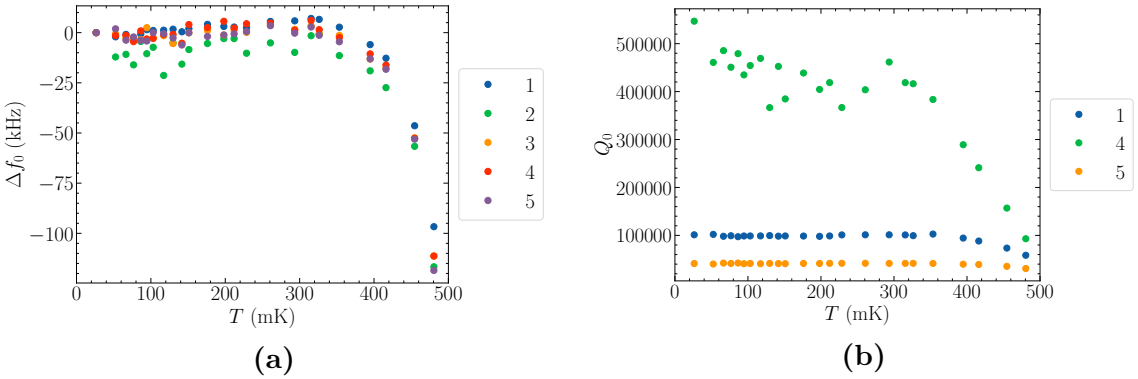

(a) **(b)**

Figure 9: Shift in f_0 and Q_0 of NitrAl resonators as a function of temperature. **(a)** Δf_0. **(b)** Q_0.

measurements has been carried out for this thesis and will be shown in this section.

Once again, the resonators were fitted by following the procedure in Appendix H. The results of the shift in resonant frequency and internal quality factor of the different resonators as a function of temperature are depicted in Figure 9, respectively. These figures show a decrease in f_0 and Q_0 with temperature, as predicted due to the action of TLS and QP. For f_0, presented in Figure 9 **(a)**, up to $T = 300$ mK, the evolution seems attributable to loss caused by TLS, as given by Equation 6. The observation of TLS in NitrAl was not obvious beforehand, since nitrides are supposed to exhibit less TLS than oxides. This implies that, besides AlN_x, there exists also AlO_x in the material. Further investigation on this topic is required.

For $T > 300$ mK, f_0 eventually experiments a much more pronounced decrease. This is explained by the saturation in TLS and the increase in the density of quasiparticles, which are, now, the main contribution to the losses of the resonators and that cause a decrease in f_0 given by Equation 7. This is also in agreement with the decrease in Q_0 that is also observed for $T > 300$ mK in Figure 9 **(b)**, as, following Equation 8, QP decrease Q_0. Since the decrease in f_0 due to QP is due to an increase in kinetic inductance, this is a sign of the superinducting qualities of NitrAl. Regarding the obtained Q_0, it is notable that they are remarkably high. For the NitrAl resonators, however, the results of resonators 2 and 3 were inconclusive, with one having $Q_0 < 0$ and the second one not following a clear progression with temperature. Those are included in Appendix J, alongside the loaded and total quality factors. This can be understood as those resonators being of poor quality. The reasons for this may be the existence of a SiO_x layer on top of the substrate that compromises resonator performance or the dissimilar properties of the different areas of the sputtered thin films. This issues will be addressed with resonators with the properties exhibited in Section 4.1 and with substrates cleaned by a few-seconds dip in 2.5% HF so as to eliminate any SiO_x layer on their surface [Ker93]. These tests, however, are beyond the scope of this thesis.

If we compare the results for NitrAl to those of pure Al (Figure 67 and also [S+20]), we can see that, although both materials follow a qualitatively comparable evolution, the decrease caused by QP in f_0 and Q_0 is not as pronounced for Al as it is for NitrAl. Additionally, it happens at a much higher temperature for NitrAl. These details might be a sign that the kinetic inductance of NitrAl, or at least its ratio to total inductance, is noticeably larger. Further work to precisely fit the right formulas to evaluate the kinetic inductance of resonators will address this.

5 Conclusions

An extended and meticulous study of NitrAl in the range were it was suspected to display higher kinetic inductance has been successfully conducted in this work. This was achieved by sputtering thin films with a 0.59 to 0.85 sccm N_2 gas flow, a 40 sccm Ar gas flow and a deposition rate of 1 Å/s.

High values of thin film resistivity were measured, which, moreover, evolved accordingly with increasing nitridation. Decreasing resistivity with thickness, however, was not clearly observed. More statistics are necessary before drawing any conclusions on this aspect. The thin film regime, in which resistivity is inversely proportional to thickness, has been found to begin below $t = 20$ nm. Hence, the metal-to-insulator transition has been demonstrated to not only be achievable by increasing N_2 in the samples, but also by decreasing thickness.

Metal-to-superconductor transitions were observed for almost all thin films, with critical temperatures ranging from 2 to 3 K. The kinetic inductance values that were estimated from them acquired values of hundreds to thousands of pH/□. This remarkably positions NitrAl as a superinductor.

Regarding the perpendicular critical field study of the films, they have been found to satisfy the expected Grinzburg-Landau dependence for $T \sim T_c$ for type-II superconductors in the dirty limit of superconductivity. From those dependencies, the mean free path and coherence length of different films were estimated. The former achieved values of 8 to 14 nm, and the latter of around a tenth of nm. These parameters are smaller for more nitridized or thinner samples, which are more resistive, in agreement with the shortened distance that electrons can freely travel in those cases because of disorder. The remarkably low values of ℓ also hint the high disorder of the samples. A difference in the behaviour of critical field depending on its orientation was spotted, confirming that for perpendicular fields superconductivity is destroyed by reaching the obital limit, whereas for parallel fields superconductivity is destroyed by the Pauli-limited effect. Although in both cases high critical fields were measured, parallel ones involved larger fields, as was also anticipated.

Critical current measurements were in the range of few mA and showed an increase with thickness. In those measurements, the disposition of the measuring probes altered the obtained values, which is consistent with disorder in the samples. This high disorder has also been identified by the different resistivity values that were measured for the same sample, which points to the existence of numerous conducting paths inside the thin films, and for some inconclusive results regarding thickness that were observed.

Although thermal annealing has been proven to lower the resistivity of films and restore oxidation, the enhancement in resistivity provoked by thermal annealing has not successfully turned insulating films into conducting ones. Additionally, from those experiments NitrAl has shown to not permanently modify its grain structure until $T = 200$°C. At that temperature, gas bubbles were observed to emanate from the material.

Additional proof of the high kinetic inductance of NitrAl has been found by means of $\lambda/4$ CPW resonators. The decrease in f_0 and Q_0 with increasing T is attributable to the action of two-level systems and quasiparticles. The latter, moreover, has brought to light further experimental evidence of the large L_{kin} of NitrAl. Nonetheless, the quality of some of the employed resonators was inconclusive. This will be addressed hereafter with the resonators designed in this work, which have a resonant frequency between 4.7 and 4.9 GHz for the expectedly high L_{kin} values and a coupling factor as close to 1 as the depth of the resonance dip allows. Additionally, substrates free from SiO_x will be employed for these devices. Conclusive results are expected on the evaluation of the intrinsic quality of NitrAl in the microwave regime as a potential material to build novel superconducting qubits.

Bibliography

[A+11] F. Arute et al. Quantum supremacy using a programmable superconducting processor. *Nature*, 574(7779):113507, Sep 2011. DOI: 10.1038/s41586-019-1666-5.

[Abr57] A. A. Abrikosov. On the magnetic properties of superconductors of the second type. *Soviet Physics - Journal of Experimental and Theoretical Physics*, 5:1174 – 1182, Jan 1957.

[AM+13] G. M. Alonzo-Medina et al. Understanding the thermal annealing process of metallic thin films. *IPO Conference Series: Materials Science and Engineering*, 45(1):012013, June 2013. DOI: 10.1088/1757-899X/45/1/012013.

[B+57] J. Bardeen et al. Theory of superconductivity. *Physical Review*, 108(5):1175, Dec 1957. DOI: 10.1103/PhysRev.108.1175.

[B+11] R. Barends et al. Minimizing quasiparticle generation from stray infrared light in superconducting quantum circuits. *Applied Physics Letters*, 99(11):113507, Sep 2011. DOI: 10.1063/1.3638063.

[B+12] M. T. Bell et al. Quantum superinductor with tunable non-linearity. *Physical Review Letters*, 109(13):137003, Sep 2012. DOI: 10.1103/PhysRevLett.109.137003.

[Doy08] S. Doyle. *Lumped Element Kinetic Inductance Detectors*. PhD thesis, University of Cardiff, 2008.

[F+23] S. Frasca et al. Nbn films with high kinetic inductance for high-quality compact superconducting resonators. *Physical Review Applied*, 20(4):044021, Oct 2023. DOI: 10.1103/PhysRevApplied.20.044021.

[Fuc38] K. Fuchs. The conductivity of thin metallic films according to the electron theory of metals. *Proceedings of the Cambridge Philosophical Society*, 34(1):100 – 108, Jan 1938. DOI: 10.1017/S0305004100019952.

[G+08] M. Göppl et al. Coplanar waveguide resonators for circuit quantum electrodynamics. *Journal of Applied Physics*, 104(11):113904, Dec 2008. DOI: 10.1063/1.3010859.

[G+19] L. Grünhaupt et al. Granular aluminium as a superconducting material for high-impedance quantum circuits. *Nature Materials*, 18(8):816 – 819, Apr 2019. DOI: 10.1038/s41563-019-0350-3.

[Gao08] J. Gao. *The Physics of Superconducting Microwave Resonators*. PhD thesis, California Institute of Technology, 2008.

[gds] https://gdspy.readthedocs.io.

[GL50] V. L. Grinzburg and L. D. Landau. On the theory of superconductivity. *Soviet Physics - Journal of Experimental and Theoretical Physics*, 20:1064, 1950.

[Gru19] L. Gruenhaupt. *Granular Aluminium Superinductors*. PhD thesis, Karlsruhe Institute of Technology, 2019.

[imi] https://scikit-hep.org/iminuit/.

[K+19] P. Krantz et al. A quantum engineer's guide to superconducting qubits. *Applied Physics Reviews*, 6(2):021318, Jun 2019. DOI: 10.1063/1.5089550.

[Ker93] W. Kern. *Handbook of Semiconductor Wafer Cleaning Technology. Science, Technology and Applications*. Noyes Publications, 1993.

[kit] https://github.com/qkitgroup/qkit.

[LB+19] F. Levy-Bertrand et al. Electrodynamics of granular aluminum from superconductor to insulator: Observation of collective superconducting modes. *Physical Review B*, 99(9):094506, Mar 2019. DOI: 10.1103/PhysRevB.99.094506.

[M+15] I. Miccoli et al. The 100th anniversary of the four-point probe technique: the role of probe geometries in isotropic and anisotropic systems. *Journal of*

Physics: Condensed Matter, 27(22):223201, May 2015. DOI: 10.1088/0953-8984/27/22/223201.

[MS70] A. F. Mayadas and F. Shatzkes. Electrical-resistivity model for polycrystalline films: the case of arbitrary reflection at external surfaces. *Physical Review B*, 1(4):1382, Feb 1970. DOI: 10.1103/PhysRevB.1.1382.

[MT64] K. Maki and T. Tsuneto. Pauli paramagnetism and superconducting state. *Progress of Theoretical Physics*, 31(6):945 – 956, June 1964. DOI: 10.1143/PTP.31.945.

[OD91] T. P. Orlando and K. A. Delin. *Foundations of Applied Superconductivity*. Addison-Wesley, 1991.

[P+11] D. P. Pappas et al. Two level system loss in superconducting microwave resonators. *IEEE Transactions on Applied Superconductivity*, 21(3):871 – 874, Jan 2011. DOI: 10.1109/TASC.2010.2097578.

[P+15] S. Probst et al. Efficient and robust analysis of complex scattering data under noise in microwave resonators. *Review of Scientific Instruments*, 86(2):024706, Feb 2015. DOI: 10.1063/1.4907935.

[Poz11] D. M. Pozar. *Microwave Engineering*. John Wiley and Sons Inc., 2011.

[R+16] H. Rotzinger et al. Aluminium-oxide wires for superconducting high kinetic inductance circuits. *Superconductor Science and Technology*, 30(2):025002, Nov 2016. DOI: 10.1088/0953-2048/30/2/025002.

[S+20] M. Scigliuzzo et al. Phononic loss in superconducting resonators on piezoelectric substrates. *New Journal of Physics*, 22(5):053027, May 2020. DOI: 10.1088/1367-2630/ab8044.

[son] https://www.sonnetsoftware.com.

[Son52] E. H. Sondheimer. The mean free path of electrons in metals. *Advances in Physics*, 1(1):1 – 42, Jan 1952. DOI: 10.1080/00018735200101151.

[TC+24] A. Torras-Coloma et al. Superconducting nitridized aluminum thin films. *Superconductor Science and Technology*, 37(3):035017, Feb 2024. DOI: 10.1088/1361-6668/ad20fc.

[Tin04] M. Tinkham. *Introduction to Superconductivity*, volume 1. Courier Corporation, 2004.

[V+10] M. R. Vissers et al. Low loss superconducting titanium nitride coplanar waveguide resonators. *Applied Physics Letters*, 97(23):232509, Dec 2010. DOI: 10.1063/1.3517252.

Appendices

A Thin film fabrication and measurement parameters

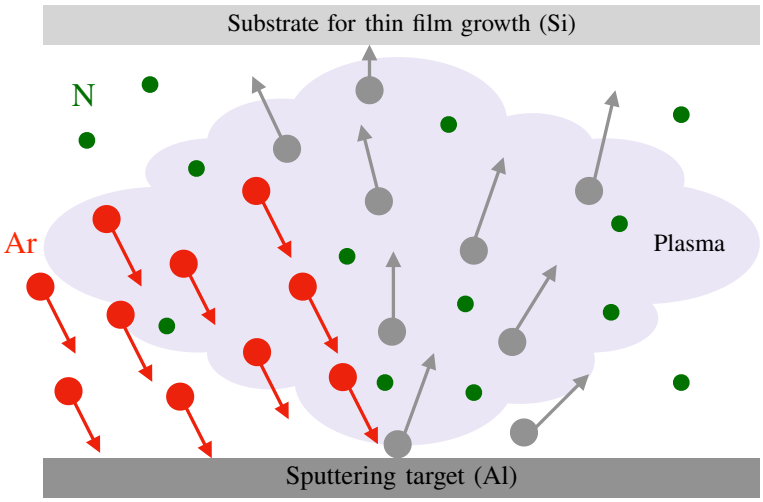

Figure 10: Schematic representation of thin film growth by sputtering in a nitrogen-rich environment for NitrAl deposition.

Sample	**N_2 (sccm)**	**Rate (Å/s)**	**t (nm)**	**P (W)**	**P_r (W)**	**V_{DC} (V)**	**P_0 (mbar)**
A	0.59	1.25	100	250	-2	-728	$5.6 \cdot 10^{-6}$
B	0.6	1	100	200	-3	-632	$2.3 \cdot 10^{-6}$
C	0.6	1	70	200	-1	-628	$2.4 \cdot 10^{-6}$
D	0.6	0.97	58	200	-3	-632	$1.2 \cdot 10^{-6}$
E	0.6	1	30	200	-1	-635	$3.1 \cdot 10^{-6}$
F	0.6	1	20	200	-1	-630	$6.2 \cdot 10^{-6}$
G	0.6	1	10	200	-1	-629	$1.9 \cdot 10^{-6}$
H	0.65	1	100	200	-2	-634	$3.4 \cdot 10^{-6}$
I	0.75	1	100	200	-1	-622	$5.0 \cdot 10^{-6}$
J	0.75	1	70	200	-1	-621	$2.6 \cdot 10^{-6}$
K	0.75	1	50	200	-1	-617	$5.3 \cdot 10^{-6}$
L	0.75	1	30	200	-1	-619	$1.6 \cdot 10^{-6}$
M	0.75	1	10	200	-1	-617	$3.1 \cdot 10^{-6}$
N	0.85	1	100	200	-1	-623	$8.2 \cdot 10^{-6}$

Table 5: Fabrication parameters of the sputtered thin film 2nd run samples. P, P_r, V_{DC} and P_0 correspond to the forwarded power, reflected power, gate voltage and sputtering chamber pressure, respectively. For all samples, the Ar gas flow was set to be 40 sccm and its pressure was $P_{\mathrm{Ar}} = 6 \cdot 10^{-3}$ mbar.

In the 1st run, samples were sputtered with a 60 sccm Ar flow and a deposition rate of 1 nm/s. The deposition rate was 10 times smaller in the 2nd run because of the size of the employed Al RF gun being considerably smaller. By that, the incorporation of N_2 in the samples seems to have been more efficient, hence achieving a higher resistivity and a

slightly lower T_c while having a comparatively smaller quantity of N_2 for the samples of the 2nd run. Because of this, the samples of the two runs are not comparable in terms of N_2/Ar gas flow during sputtering ratio (note that, for the 2nd run samples, it is of the order of 1%). This also points out the difficulty in reproducing films in different fabrication runs, just as happens with grAl.

Sample	**N_2 (sccm)**	**t (nm)**	**w (mm)**	**l_V (mm)**	**A (mm^2)**
A	0.59	100	2.6	4.1	$2.6 \cdot 10^{-4}$
B	0.6	100	3.5	4.8	$3.5 \cdot 10^{-4}$
C	0.6	70	2.9	4.6	$2.03 \cdot 10^{-4}$
D	0.6	58	5	3.5	$2.9 \cdot 10^{-4}$
E	0.6	30	2.6	4.6	$7.8 \cdot 10^{-5}$
F	0.6	20	2.6	3.4	$5.2 \cdot 10^{-5}$
G	0.6	10	2.5	3.8	$2.5 \cdot 10^{-5}$
H	0.65	100	3.28	3.98	$3.28 \cdot 10^{-4}$
I	0.75	100	2.9	3.7	$2.9 \cdot 10^{-4}$
J	0.75	70	2.8	3.5	$1.96 \cdot 10^{-4}$
K	0.75	50	2.72	4.0	$1.4 \cdot 10^{-4}$
L	0.75	30	3	2.6	$9 \cdot 10^{-5}$
M	0.75	10	2.2	3.5	$2.2 \cdot 10^{-5}$
N	0.85	100	2.6	4.3	$2.6 \cdot 10^{-4}$

Table 6: Measurement parameters of the sputtered thin film 2nd run samples. w, l_V and A correspond to the width of the samples, the distance between the voltage wires and the cross-section of the samples, respectively. A is calculated as $w \cdot t$.

B Totality of resistivity curves

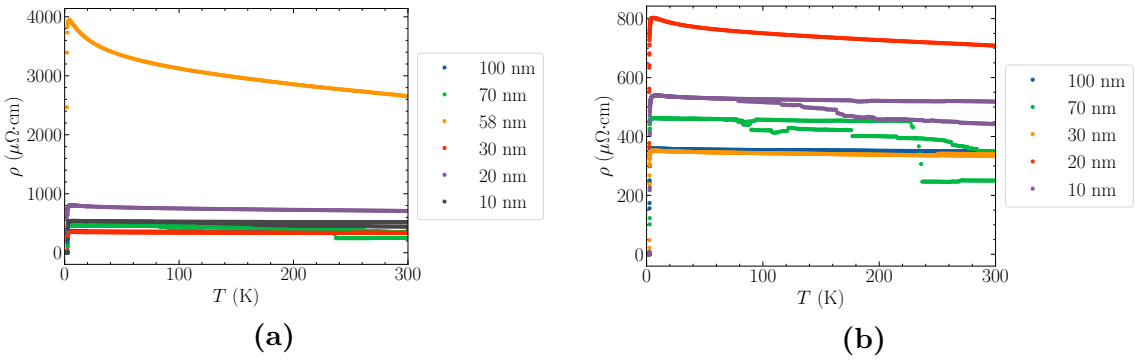

Figure 11: Resistivity curves obtained for the 2nd run samples sputtered with a 0.6 sccm N_2 gas flow. **(a)** All samples. **(b)** Less resistive samples.

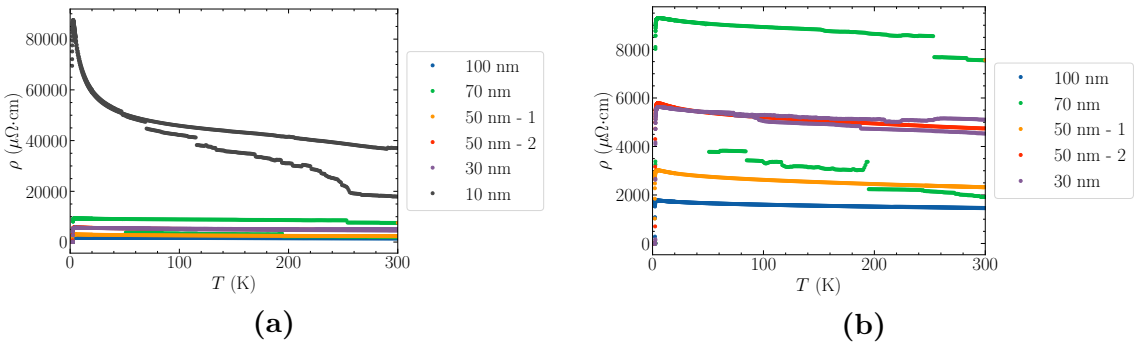

Figure 12: Resistivity curves obtained for the 2nd run samples sputtered with a 0.75 sccm N_2 gas flow. **(a)** All samples. **(b)** Less resistive samples.

The curve corresponding to $t = 58$ nm in Figure 11 **(a)**, which reaches much higher values, can be disregarded, as it corresponds to one of the samples that was fabricated during the first trials for calibration and therefore may be misleading.

C Wire-bonding methods discussion

Two different methods were tried to perform the cryogenic measurement of the 2nd run samples:

- Al wires, directly bonded onto the sample's surface.
- Cu wires, secured onto the sample's surface with Ag conducting epoxy resin.

Visual examples of the two wire-bonding versions are presented in Figure 13 for better understanding.

The cause behind trying two different techniques was the fact that, during cool-down, some of the Al contacts were lost, probably because of He pumping. This impeded the completion of the measurement of several samples. For this reason, it was decided to switch to Ag/Cu wire-bonding.

This second method is much more reliable and secure in terms of electrical contact. Nonetheless, it has some flaws. Apart from the obvious increase in time consumption that Ag/Cu wire-bonding involves, the process needs for the samples to be baked at 120°C for about 15 minutes so as to solidify the resin. From the thermal annealing experiments performed for this thesis, we learnt that for temperatures below 200°C NitrAl recovers its pre-bake resistivity values, and therefore the performance of the bakes for the solidification of the Ag epoxy resin should not affect the samples. Nevertheless, it would be desirable not to perform any thermal treatment on the films to better preserve their native attributes. Moreover, if the bake is not accurately performed, the epoxy resin might not be completely solidified by the end of the procedure. This can lead to a poor electrical contact, which then produces unreliable sample measurements.

A comparison of different samples measured twice with the two different methods is depicted in Figures 14 and 15. As can be seen, at high temperatures (generally above $T = 200$ K), the curves measured via Ag/Cu bonds present some resistivity jumps: generally, resistivity during cooldown for samples wire-bonded with AG/Cu was smaller than during heatup. This has been observed in several resistivity curves presented in this thesis, and it even impeded us to infer the room temperature resistivity in some cases. However, at low temperatures (below $T = 20$ K), the data follows a good and seemingly reliable evolution. There is a difference in the measured resistivity values in each case. The different values are, nonetheless, of the same order of magnitude. In any case, this last fact cannot be fully attributable to wire-bonding, since, as it has been mentioned at several points in this thesis, the microscopical disorder and various conducting paths of the samples are the most likely cause.

Due to the resistivity jumps observed at high temperature when employing Ag/Cu bonds and the easiness of the Al wire-bonding process, it was decided to use the Al approach in general, and only use Ag/Cu bonds when the first method failed.

An interesting fact that was observed after the usage of the two different types of bonds is that, after removing the Ag epoxy resin contacts, the NitrAl thin film was also released from the Si substrate. This implies that the subjection of the sputtered film onto the used substrates was not optimal. This inconvenience might also be behind the jumps in resistivity during cool-down and the differences in resistivity for the same samples sputtered and/or measured multiple times, alongside the previously mentioned justifications.

(a) **(b)**

Figure 13: Examples of the different used wire-bonding approaches for the 2nd run samples. **(a)** Al wires. **(b)** Cu wires, secured via Ag epoxy.

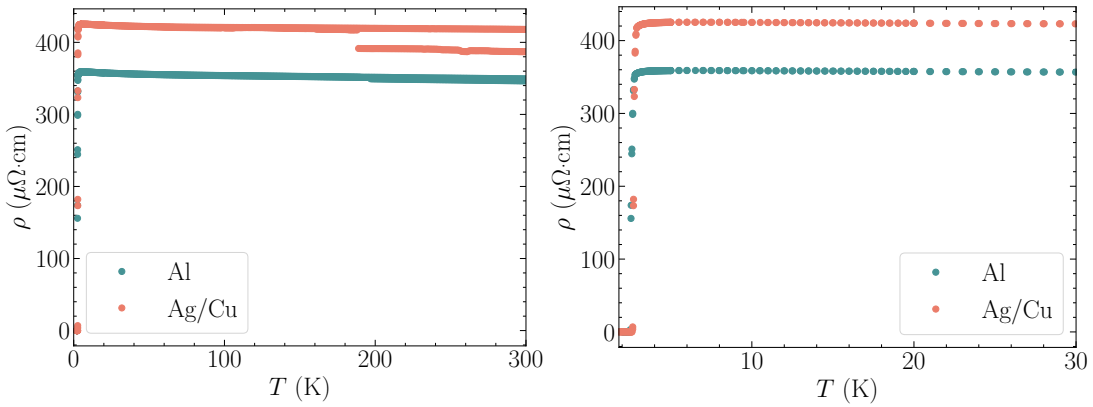

(a) **(b)**

Figure 14: Comparison between the resistivity curves obtained with different wire-bonding methods for a sample sputtered with a 0.6 sccm N_2 gas flow and a thickness of 100 nm. **(a)** Curve from $T = 300$ K to $T = 1.8$ K. **(b)** Curve from $T = 30$ K to $T = 1.8$ K.

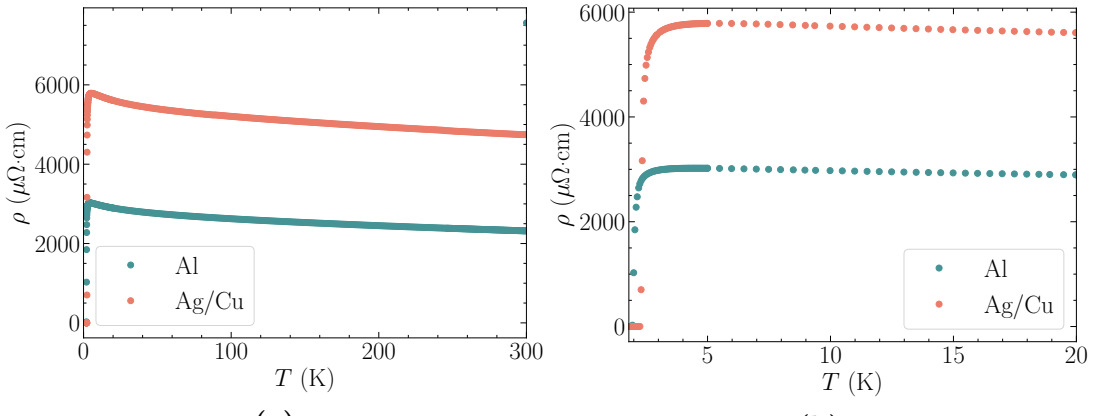

(a) **(b)**

Figure 15: Comparison between the resistivity curves obtained with different wire-bonding methods for a sample sputtered with a 0.75 sccm N_2 gas flow and a thickness of 50 nm. **(a)** Curve from $T = 300$ K to $T = 1.8$ K. **(b)** Curve from $T = 20$ K to $T = 1.8$ K.

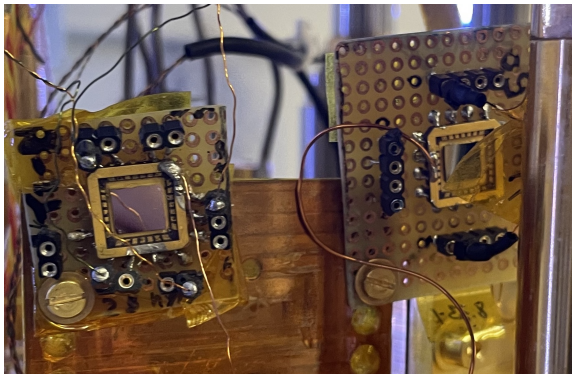

Figure 16: Wire-bonding method pursued at IFAE to measure 1st run samples at cryogenic temperatures.

D Critical temperature: estimation method, raw data and parameter fitting

From the measurement of the samples, T_c was obtained by fitting the raw data at temperatures below 4 K as

$$\rho = \frac{A}{2} \tanh\left[B\left(T - T_c\right)\right] + C. \tag{9}$$

In this equation, A corresponds to the amplitude of the curve (that is, resistivity at $T = 4$ K), B is a parameter to account for the sharpness of the transition and C is included so as to account for possible offsets in resistivity (that is, resistivity having values larger than 0 after the transition). After an initial guess, the three values are fitted by using the `curve_fit` SciPy function, which employs the least-square methods. The uncertainty in T_c was computed as the uncertainty in the fit; that is, the square root of the corresponding diagonal element of the covariance matrix that the `curve_fit` function outputs.

T_c, however, is usually computed from raw data following a different approach. It is typically fitted by doing a linear regression of the resistivity close to 4 K and close to 0 K, computing when the values close to the expected T_c differ by a 10% of each line and taking the mid value of the remaining points as the critical temperature. Another alternative ordinary approach is to compute the gradient $\mathrm{d}\rho/\mathrm{d}T$ and looking for the points where the gradient is more pronounced. Nonetheless, the fitting of the hyperbolic tangent was used instead of the traditional methods because of the high dispersion of some of the raw data, particularly that of the samples with lower critical temperature. This dispersion origins in the difficulty to reach, control, and maintain temperatures below 2 K, as the employed BlueFors SD refrigerator is not designed to operate at between 1 and 3 K. A second possible cause for this are the aforementioned different conducting paths inside the samples, which might have different critical temperatures and therefore give rise to different superimposed transition curves.

Figures 17 and 18 show the different metal-to-superconductor transition curves and their corresponding parameter fits.

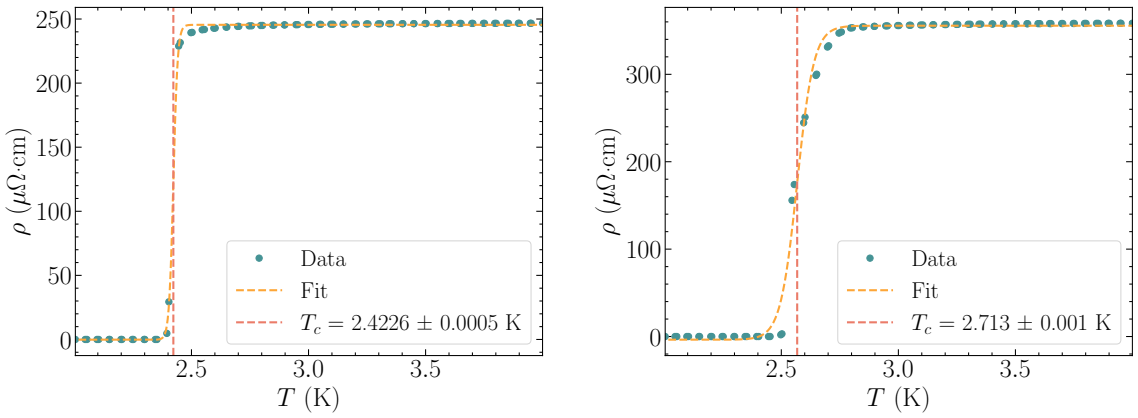

(a) **(b)**

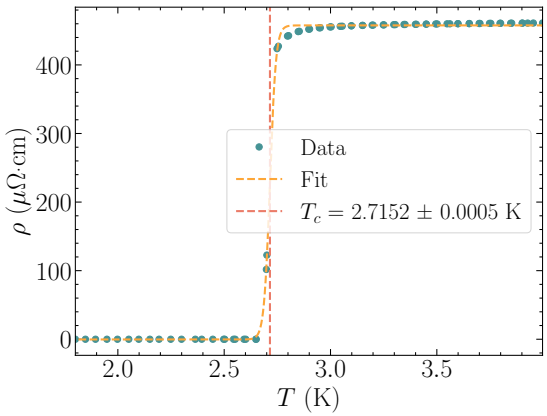
Data
Fit
$T_c = 2.7152 \pm 0.0005$ K
ρ ($\mu\Omega$·cm)
T (K)

(c)

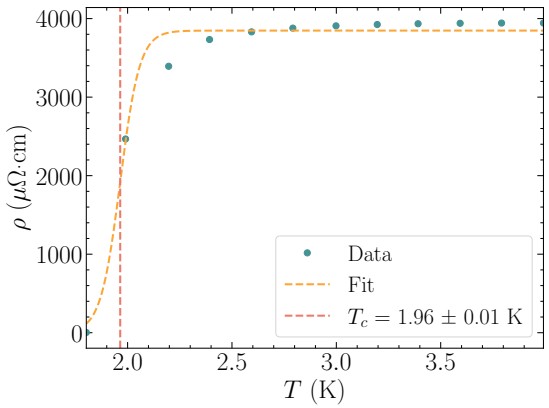
Data
Fit
$T_c = 1.96 \pm 0.01$ K
ρ ($\mu\Omega$·cm)
T (K)

(d)

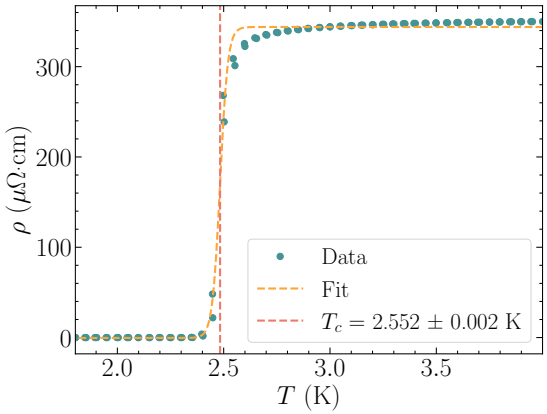
Data
Fit
$T_c = 2.552 \pm 0.002$ K
ρ ($\mu\Omega$·cm)
T (K)

(e)

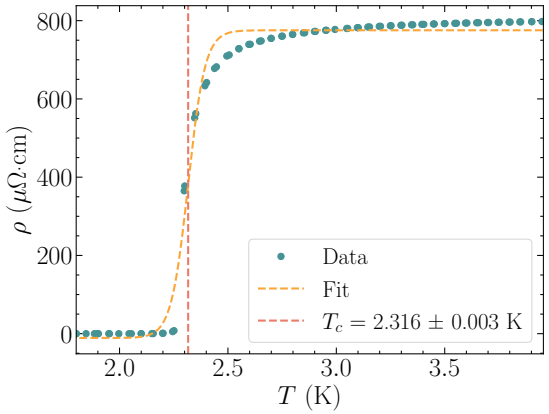
Data
Fit
$T_c = 2.316 \pm 0.003$ K
ρ ($\mu\Omega$·cm)
T (K)

(f)

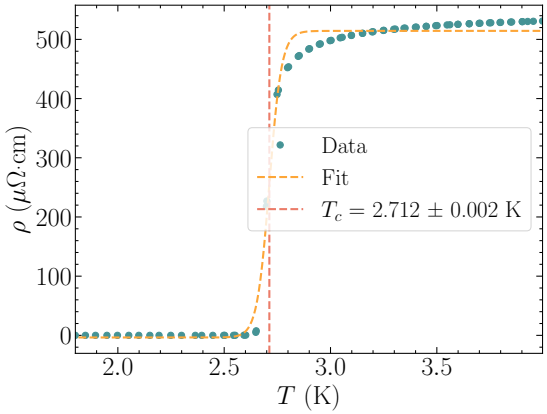
Data
Fit
$T_c = 2.712 \pm 0.002$ K
ρ ($\mu\Omega$·cm)
T (K)

(g)

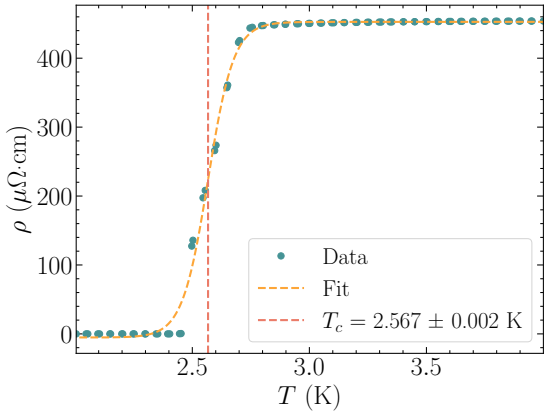
Data
Fit
$T_c = 2.567 \pm 0.002$ K
ρ ($\mu\Omega$·cm)
T (K)

(h)

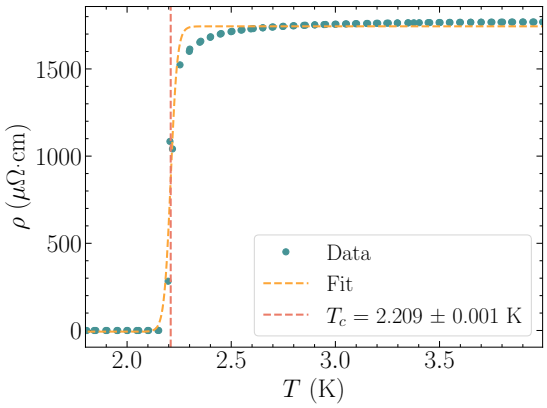
1500
1000
500
0
ρ (μΩ·cm)
2.0
2.5
3.0
3.5
T (K)
Data
Fit
$T_c = 2.209 \pm 0.001$ K

(i)

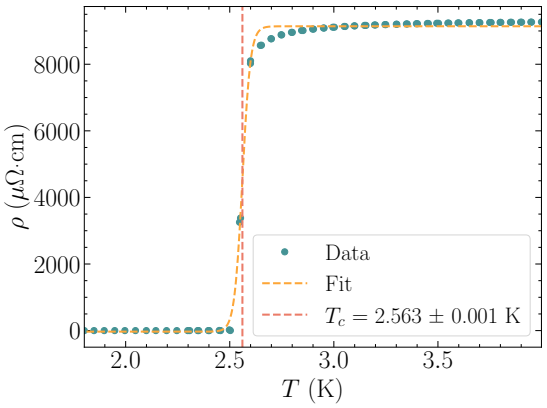
8000
6000
4000
2000
0
ρ (μΩ·cm)
2.0
2.5
3.0
3.5
T (K)
Data
Fit
$T_c = 2.563 \pm 0.001$ K

(j)

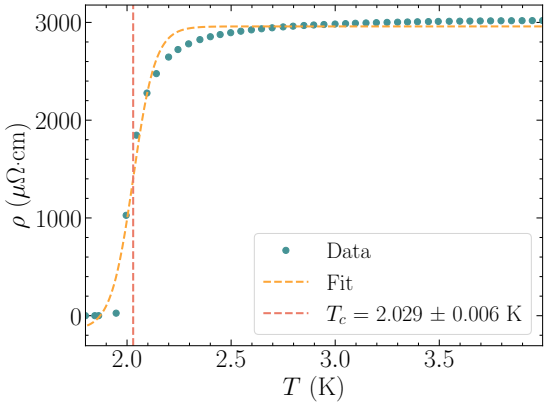
3000
2000
1000
0
ρ (μΩ·cm)
2.0
2.5
3.0
3.5
T (K)
Data
Fit
$T_c = 2.029 \pm 0.006$ K

(k)

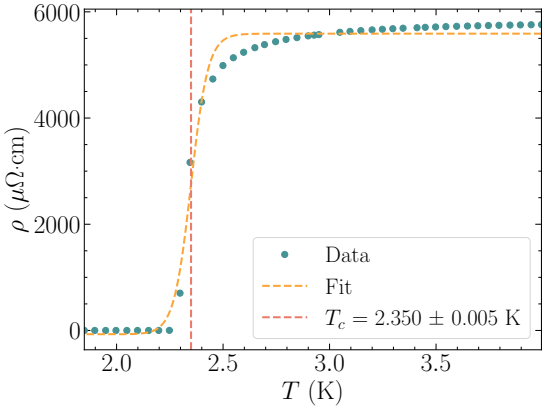
6000
4000
2000
0
ρ (μΩ·cm)
2.0
2.5
3.0
3.5
T (K)
Data
Fit
$T_c = 2.350 \pm 0.005$ K

(l)

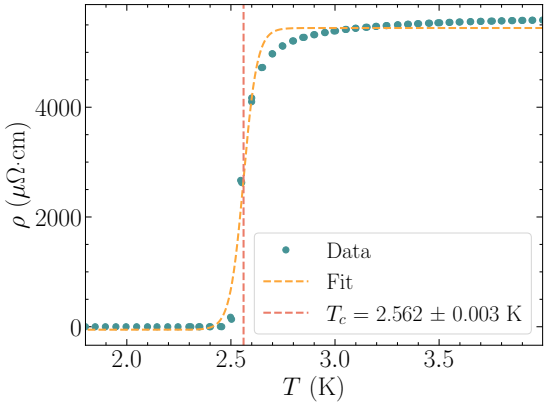
4000
2000
0
ρ (μΩ·cm)
2.0
2.5
3.0
3.5
T (K)
Data
Fit
$T_c = 2.562 \pm 0.003$ K

(m)

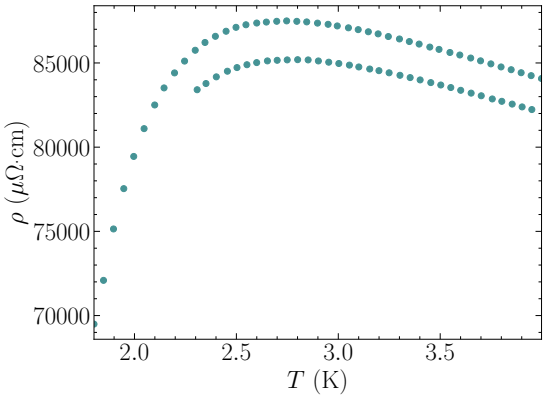
85000
80000
75000
70000
ρ (μΩ·cm)
2.0
2.5
3.0
3.5
T (K)

(n)

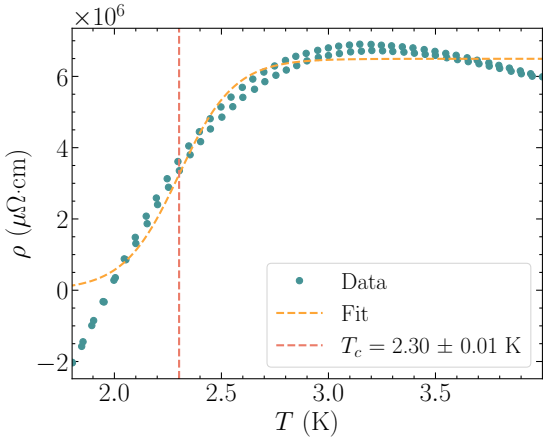

(o)

Figure 17: Resistivity below $T = 4$ K and critical temperature fitting for the different studied 2nd run samples. **(a)** Sample A. **(b)** Sample B. **(c)** Sample C. **(d)** Sample D. **(e)** Sample E. **(f)** Sample F. **(g)** Sample G. **(h)** Sample H. **(i)** Sample I. **(j)** Sample J. **(k)** Sample K - 1. **(l)** Sample K - 2. **(m)** Sample L. **(n)** Sample M. **(o)** Sample N.

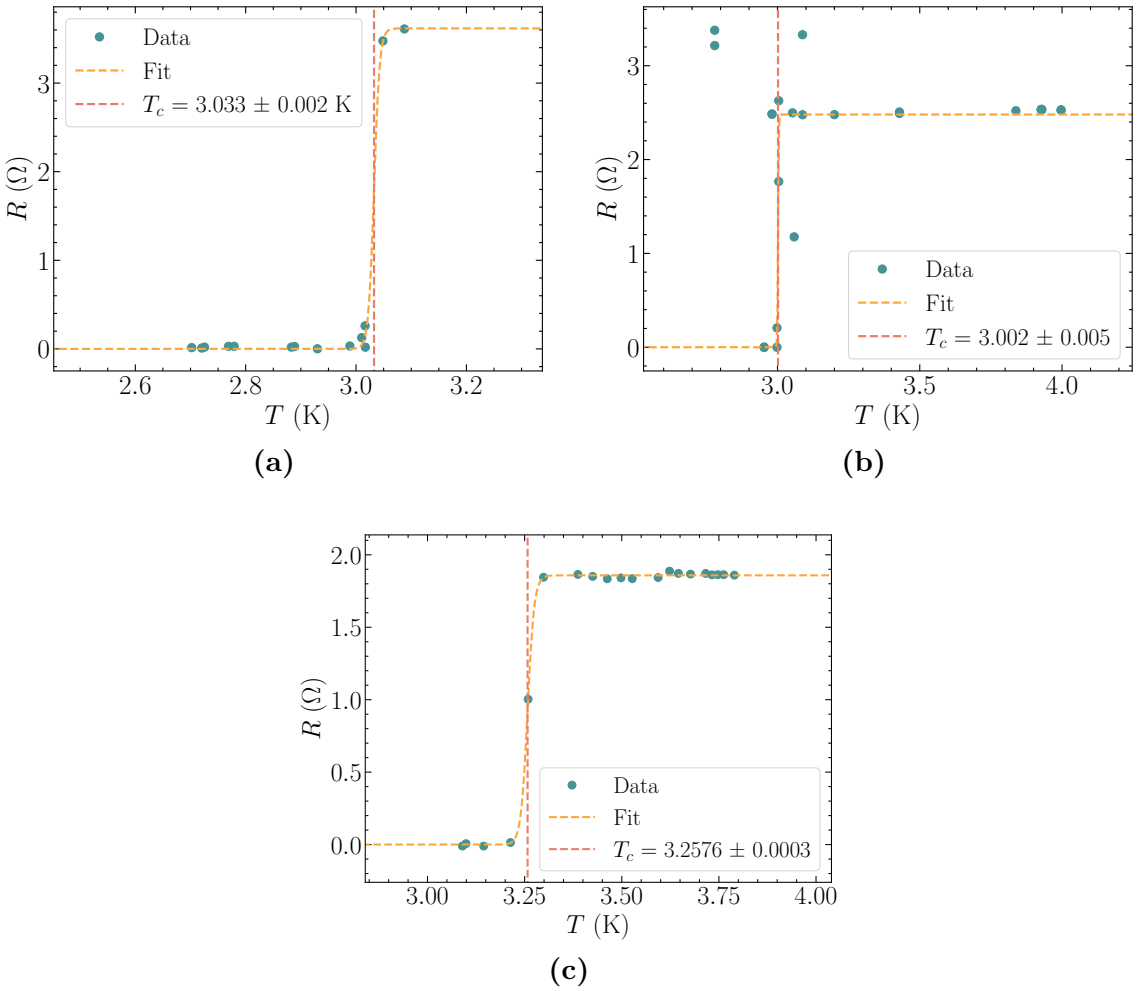

Figure 18: Resistance below $T = 4$ K and critical temperature fitting for the different studied 1st run samples, all sputtered with a 5% N_2/Ar gas flow ratio. **(a)** $t = 25$ nm, C1. **(b)** $t = 25$ nm, C2. **(c)** $t = 50$ nm, C1.

Figure 18 **(b)** is a good example of the dispersion in the measurements that forced us to use the modified hyperbolic tangent for the parameter fitting instead of other methods.

It is noteworthy that, in general, all samples experience a sharp metal-to-superconductor transition, as desired for conducting samples. Only the samples in Figure 17 **(d)**, **(n)** and **(o)** experience blunt transitions. This is a sign of those samples being close to the metal-to-insulator transition, as their high resistivity and low critical temperature also point out.

E Critical field: measurement approaches and raw data

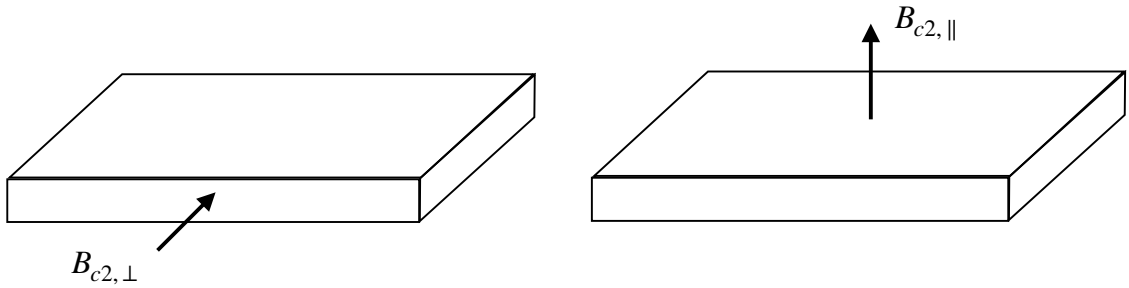

(a) **(b)**

Figure 19: Different directions of application of external magnetic fields. **(a)** Perpendicular field. **(b)** Parallel field.

The determination of B_{c2} was accomplished by applying an external magnetic field to the samples and measuring their critical temperature under that modified conditions (that is, a temperature scan was performed). This is contrary to what was explained in Section 2.1.3. There, an approach consisting on applying enlarging magnetic fields at temperatures below T_c was suggested. This technique is known as subjecting the samples to a field scan. While both methods are equivalent and lead to equal results, the pursued approach was more suited for our setup. To address the reciprocity of the two kinds of measurements, both were carried out and compared for two of the studied samples.

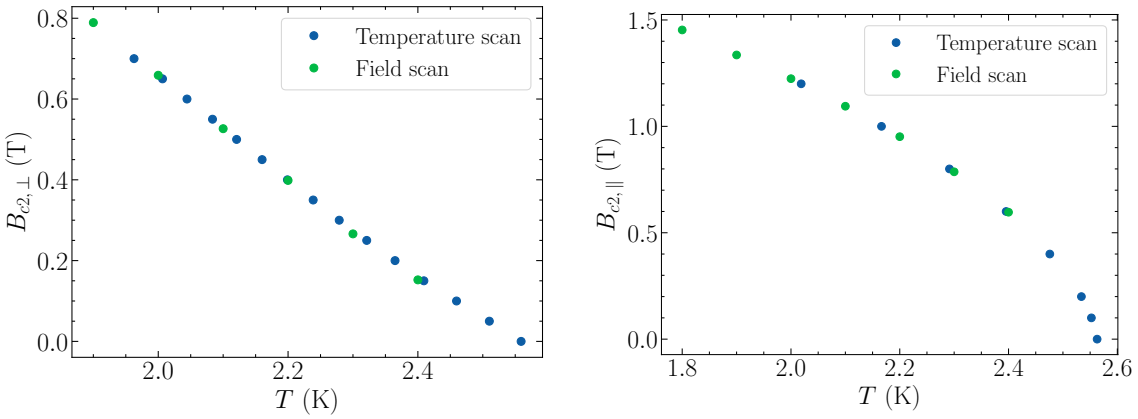

(a) **(b)**

Figure 20: Results of the different B_{c2} measurement approaches for the 2nd run sample sputtered with a 0.75 sccm N_2 gas flow and a thickness of 70 nm. **(a)** Perpendicular field. **(b)** Parallel field.

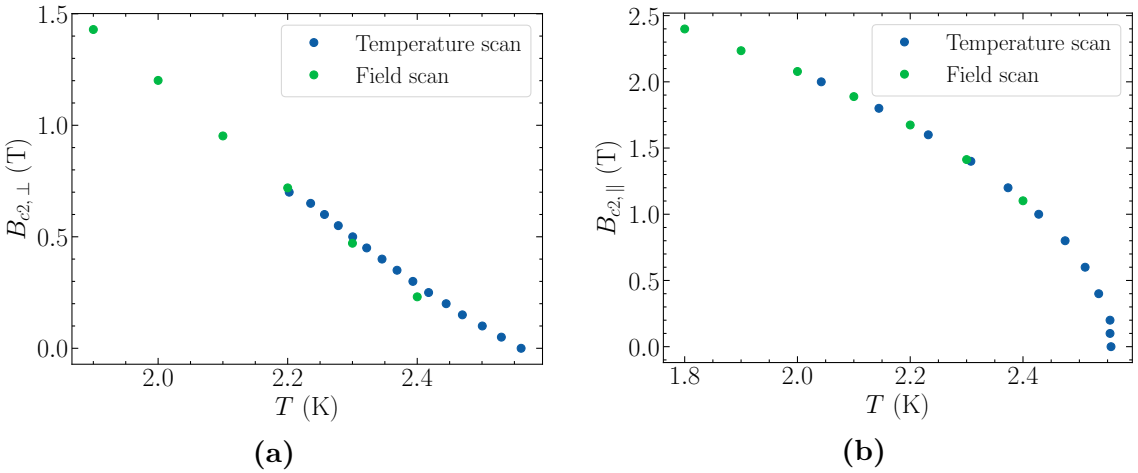

Figure 21: Results of the different B_{c2} measurement approaches for the 2nd run sample sputtered with a 0.75 sccm N_2 gas flow and a thickness of 30 nm. **(a)** Perpendicular field. **(b)** Parallel field.

Sample	t **(nm)**	**Scan**	**Slope (T/K)**	$\xi_{GL}(0)$ **(nm)**	ℓ **(nm)**
J	70	Temperature	-1.19 ± 0.02	10.38 ± 0.07	0.092 ± 0.001
J	70	Field	-1.28 ± 0.01	10.01 ± 0.05	0.0856 ± 0.0009
L	30	Temperature	-2.01 ± 0.03	7.99 ± 0.06	0.0457 ± 0.002
L	30	Field	-2.40 ± 0.02	7.31 ± 0.02	0.0457 ± 0.0002

Table 7: Magnitudes derived from the perpendicular field and temperature scans of two of the samples sputter with a 0.75 sccm N_2 gas flow. The slopes correspond to the linear regressions of Figures 20 **(a)** and 21 **(a)**, and the uncertainties have been derived as explained previously in this work.

The highly similar behaviours shown in Figures 20 and 21 and the comparable slopes, mean free paths and coherence lengths presented in Table 7 that are derived from the perpendicular field dependencies for the two types of scans prove their equivalence.

Figures 22 to 38 show the numerous metal-to-superconductor transition resistivity curves that were measured under different magnetic fields, and from which Figures 5 and 6 were extracted. Due to their similar behaviour, those where fitted following the same modified hyperbolic tangent method that was used for T_c.

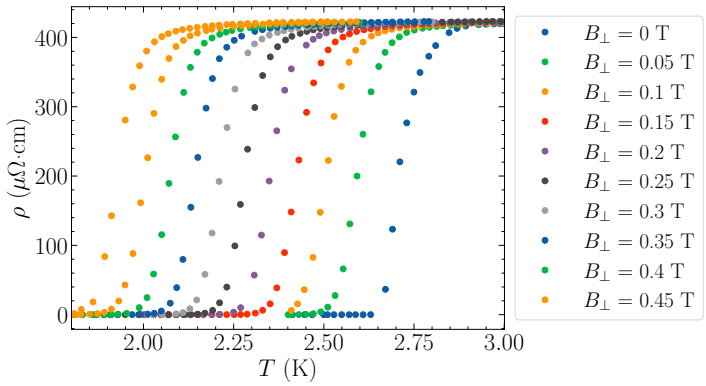

Figure 22: Resistivity curves for $T < 3$ K of the 2nd run sample of $t = 100$ nm fabricated with a 0.6 sccm N_2 under various external perpendicular magnetic fields.

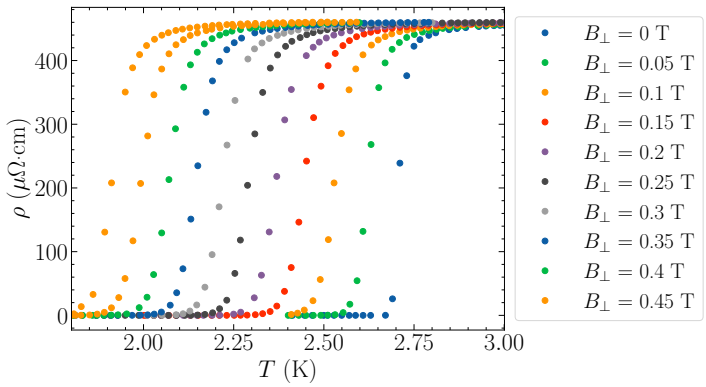

Figure 23: Resistivity curves for $T < 3$ K of the 2nd run sample of $t = 70$ nm fabricated with a 0.6 sccm N_2 gas flow under various external perpendicular magnetic fields.

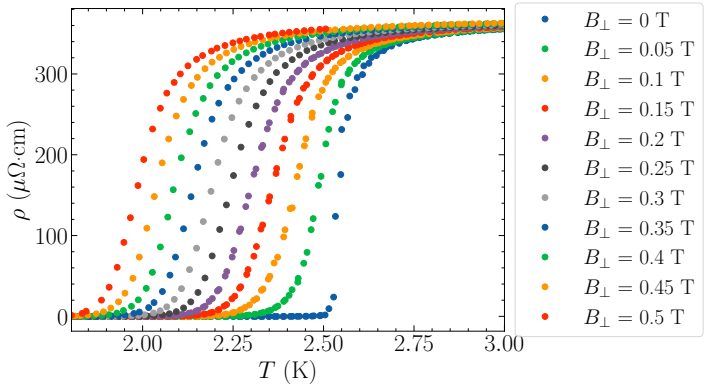

Figure 24: Resistivity curves for $T < 3$ K of the 2nd run sample of $t = 30$ nm fabricated with a 0.6 sccm N_2 gas flow under various external perpendicular magnetic fields.

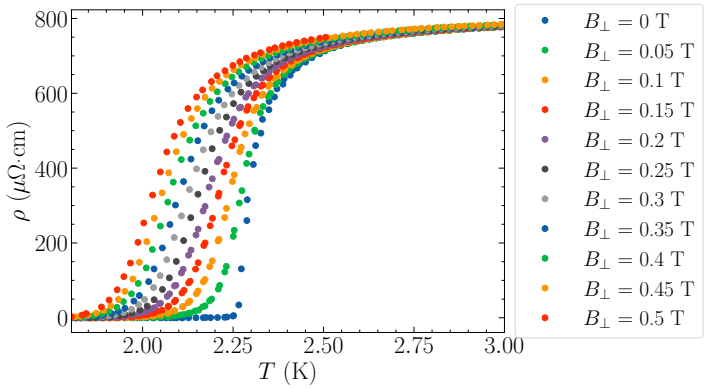

Figure 25: Resistivity curves for $T < 3$ K of the 2nd run sample of $t = 20$ nm fabricated with a 0.6 sccm N_2 gas flow under various external perpendicular magnetic fields.

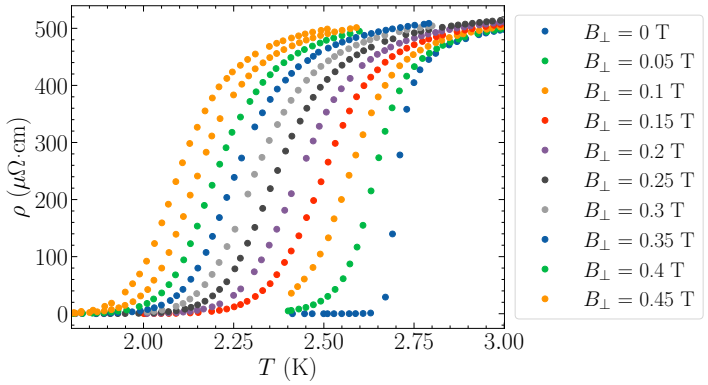

Figure 26: Resistivity curves for $T < 3$ K of the 2nd run sample of $t = 10$ nm fabricated with a 0.6 sccm N_2 gas flow under various external perpendicular magnetic fields.

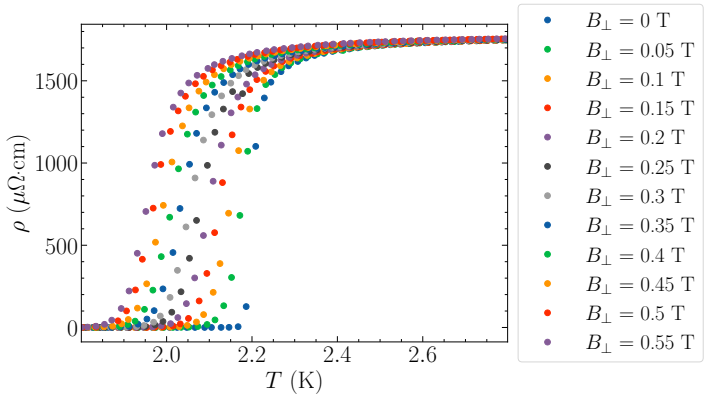

Figure 27: Resistivity curves for $T < 3$ K of the 2nd run sample of $t = 100$ nm fabricated with a 0.75 sccm N_2 gas flow under various external perpendicular magnetic fields.

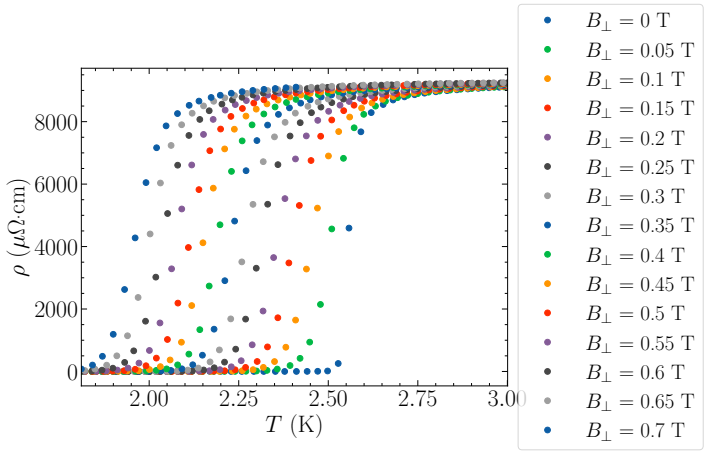

Figure 28: Resistivity curves for $T < 3$ K of the 2nd run sample of $t = 70$ nm fabricated with a 0.75 sccm N_2 gas flow under various external perpendicular magnetic fields.

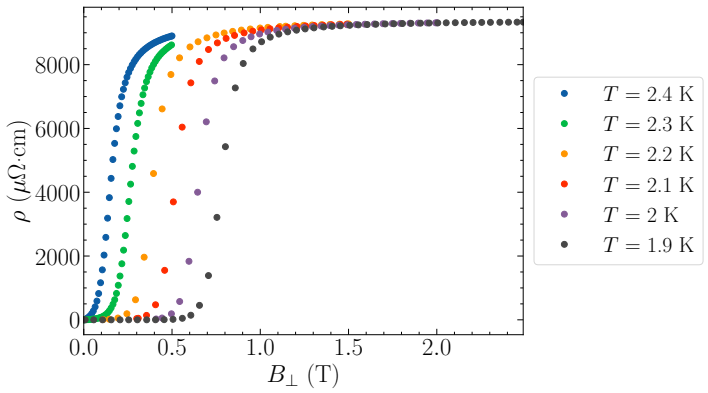

Figure 29: Resistivity curves as a function of the applied perpendicular magnetic field of the 2nd run sample of $t = 70$ nm fabricated with a 0.75 sccm N_2 gas flow in various temperatures.

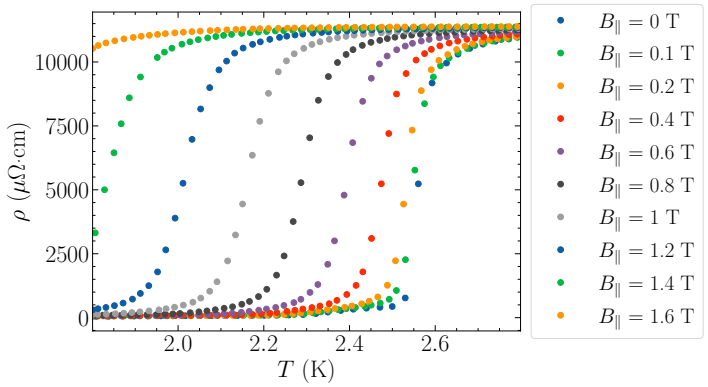

Figure 30: Resistivity curves for $T < 3$ K of the 2nd run sample of $t = 70$ nm fabricated with a 0.75 sccm N_2 gas flow under various external parallel magnetic fields.

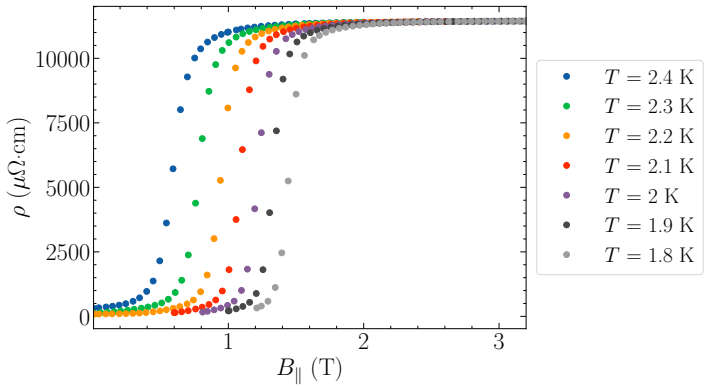

Figure 31: Resistivity curves as a function of the applied parallel magnetic field of the 2nd run sample of $t = 70$ nm fabricated with a 0.75 sccm N_2 gas flow in various temperatures.

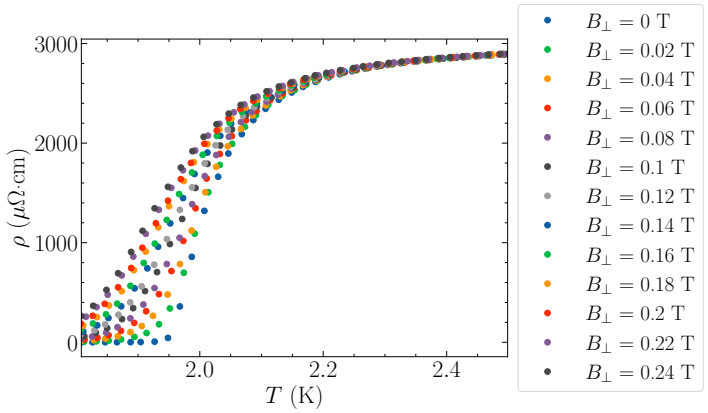

Figure 32: Resistivity curves for $T < 3$ K of the 2nd run sample of $t = 50$ nm fabricated with a 0.75 sccm N_2 gas flow under various external perpendicular magnetic fields.

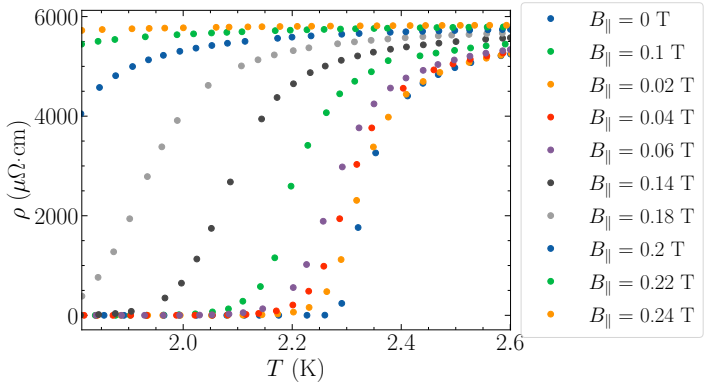

Figure 33: Resistivity curves for $T < 3$ K of the 2nd run sample of $t = 50$ nm fabricated with a 0.75 sccm N_2 gas flow under various external parallel magnetic fields.

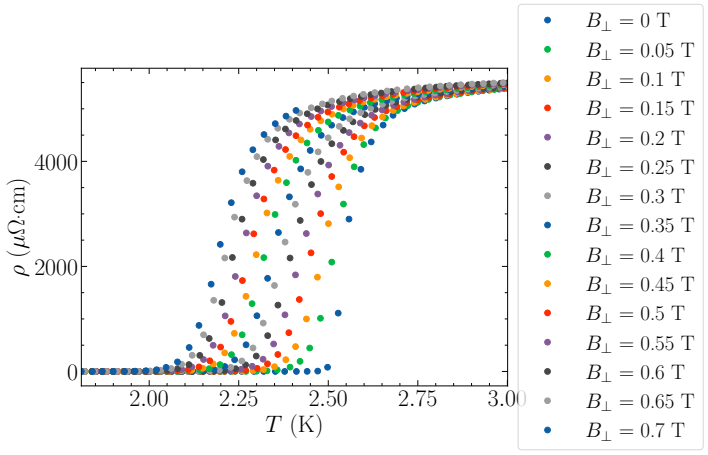

Figure 34: Resistivity curves for $T < 3$ K of the 2nd run sample of $t = 30$ nm fabricated with a 0.75 sccm N_2 gas flow under various external perpendicular magnetic fields.

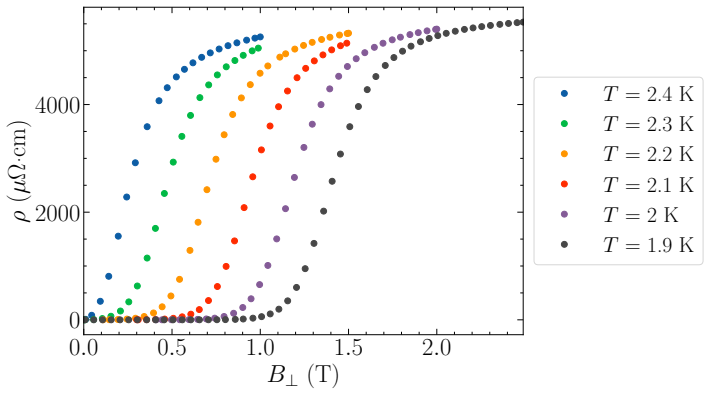

Figure 35: Resistivity curves as a function of the applied perpendicular magnetic field of the 2nd run sample of $t = 30$ nm fabricated with a 0.75 sccm N_2 gas flowin various temperatures.

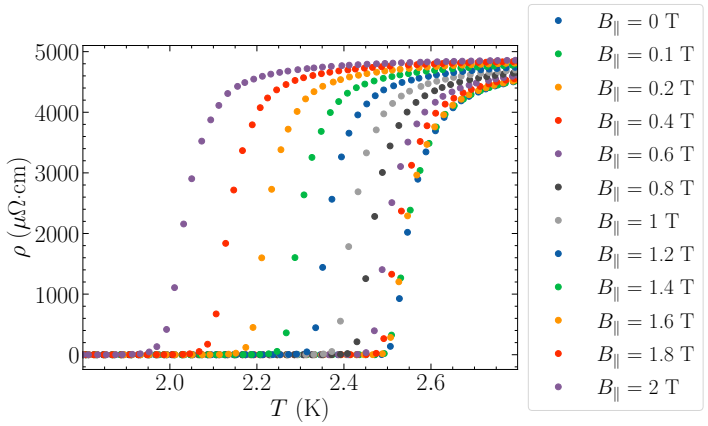

Figure 36: Resistivity curves for $T < 3$ K of the 2nd run sample of $t = 30$ nm fabricated with a 0.75 sccm N_2 gas flow under various external parallel magnetic fields.

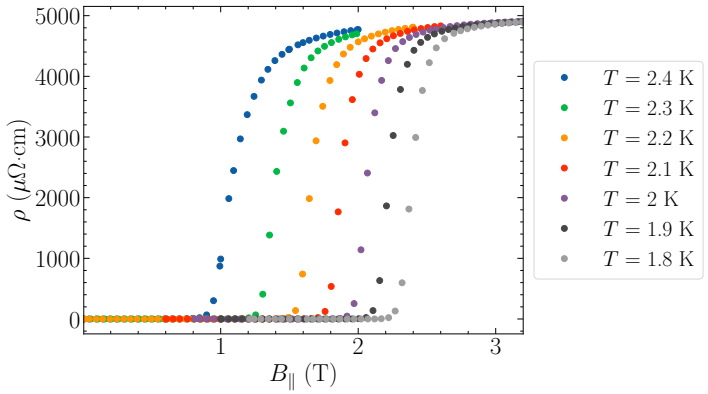

Figure 37: Resistivity curves as a function of the applied parallel magnetic field of the 2nd run sample of $t = 30$ nm fabricated with a 0.75 sccm N_2 gas flow in various temperatures.

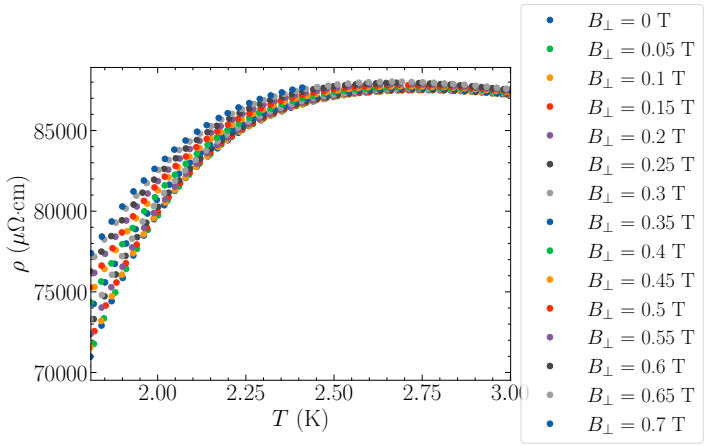

Figure 38: Resistivity curves for $T < 3$ K of the 2nd run sample of $t = 10$ nm fabricated with a 0.75 sccm N_2 gas flow under various external parallel magnetic fields.

F Critical current: raw data and parameter fitting

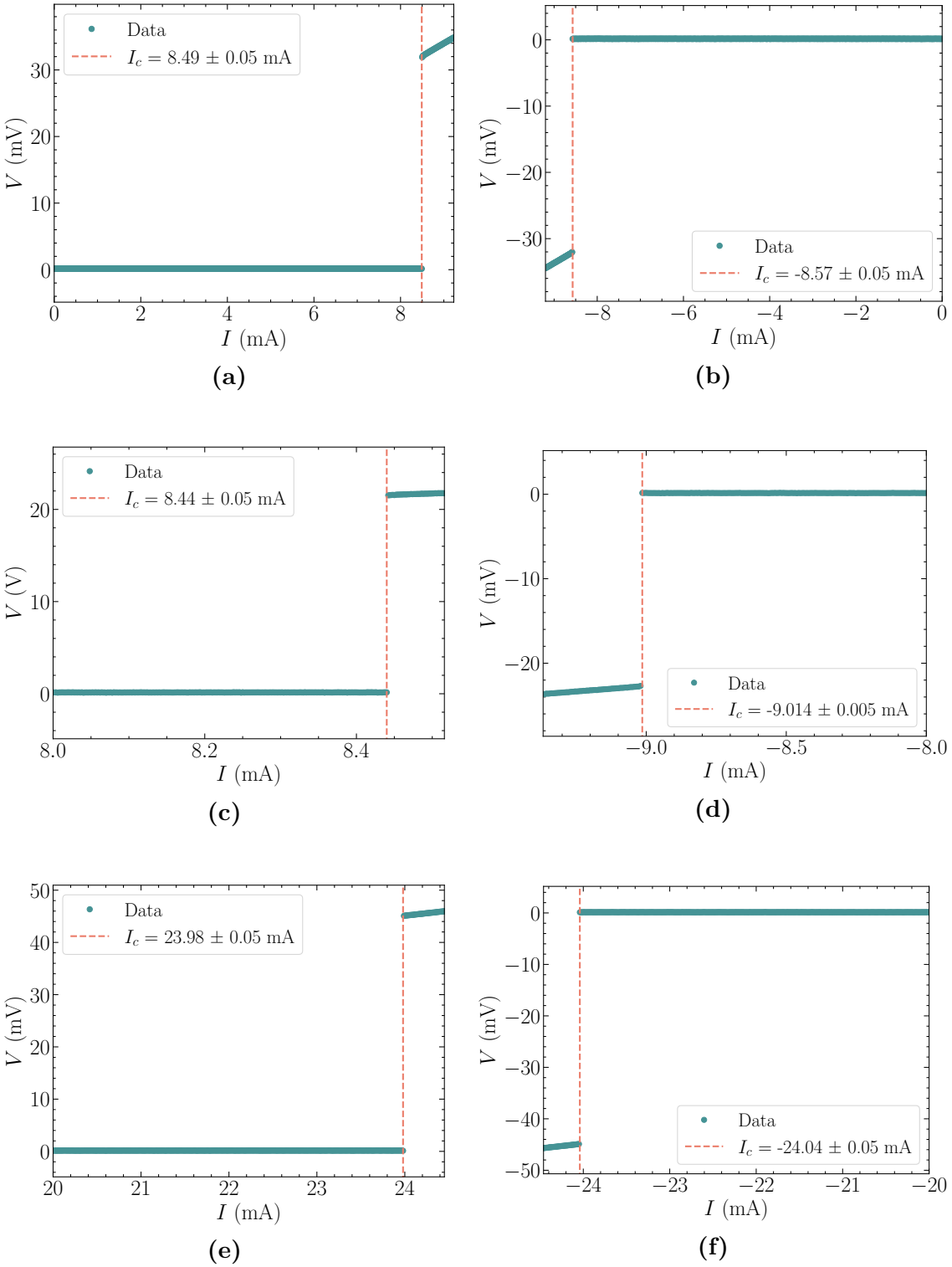

Figure 39: $I - V$ curves for the study of the critical current of 1st run samples sputtered with a 5% N_2/Ar gas flow ratio. **(a)** t = 25 nm, C1, positive current. **(b)** t = 25 nm, C1, negative current. **(c)** t = 25 nm, C2, positive current. **(d)** t = 25 nm, C2, negative current. **(e)** t = 50 nm, positive current. **(f)** t = 50 nm, negative current.

G Thermal annealing of grAl, Al and NitrAl (13.3% and 15%) thin films

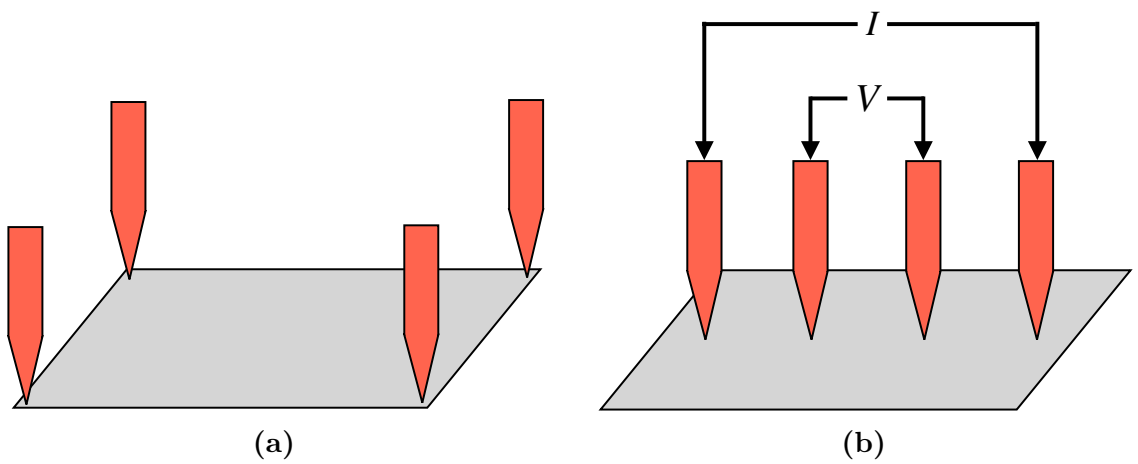

Figure 40: Different probe configurations for the measurement of resistance, sheet resistance and resistivity. **(a)** Van der Pauw method, employed to measure 1st run samples. **(b)** Collinear configuration, employed to measure 2nd run samples.

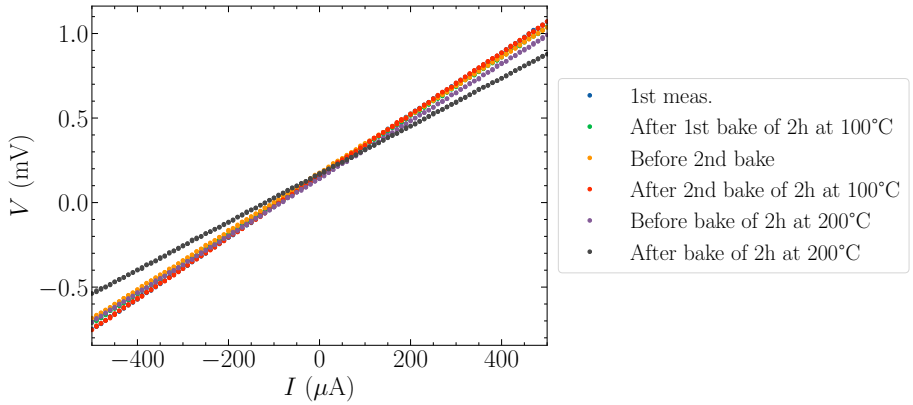

Figure 41: $I - V$ curves of the 1st grAl sample of $t = 100$ nm during the consecutive thermal annealing treatments.

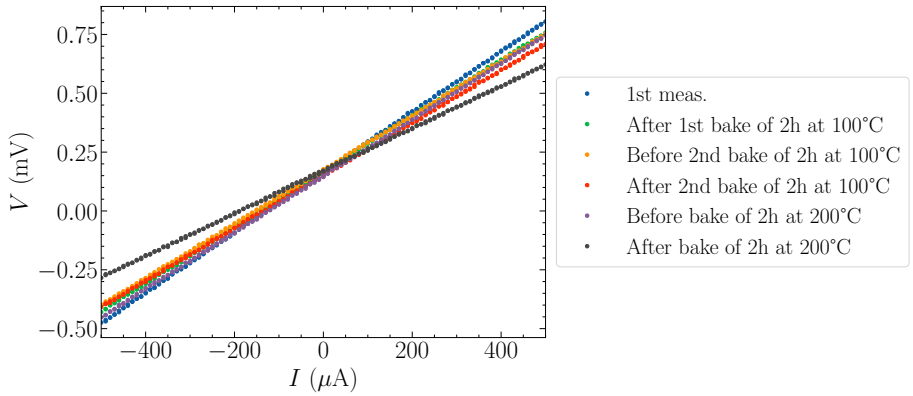

Figure 42: $I - V$ curves of the 1st grAl sample of $t = 100$ nm, rotated by 90°, during the consecutive thermal annealing treatments.

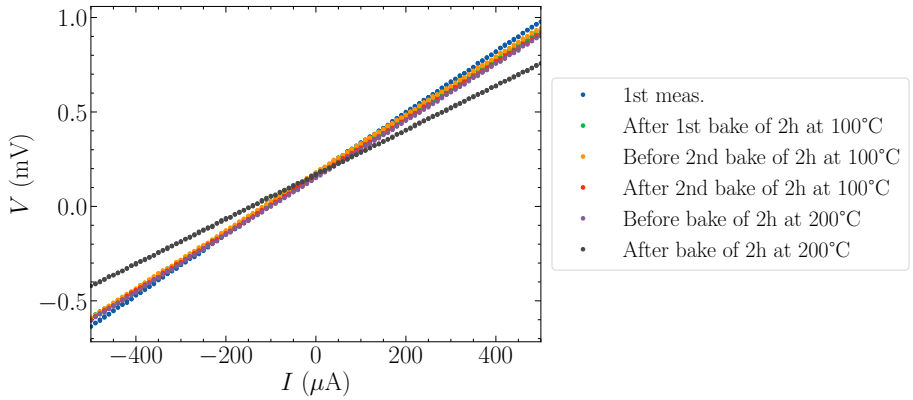

Figure 43: $I - V$ curves of the 2nd grAl sample of $t = 100$ nm during the consecutive thermal annealing treatments.

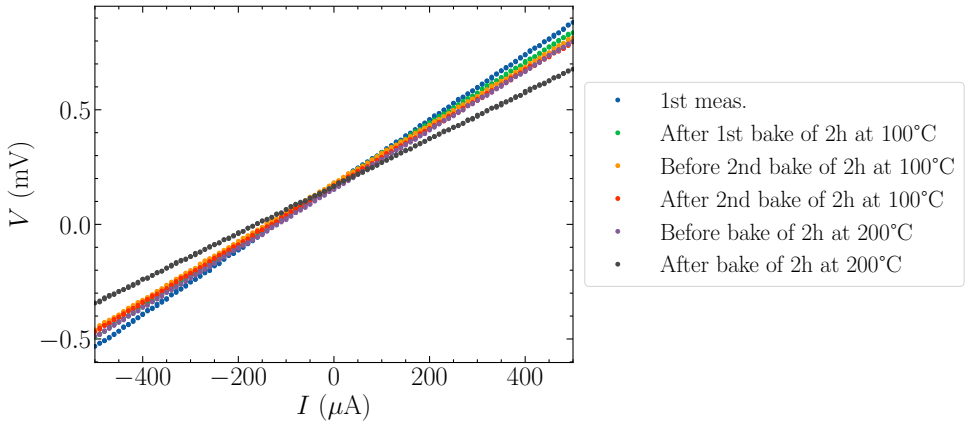

Figure 44: $I - V$ curves of the 2nd grAl sample of $t = 100$ nm, rotated by 90°, during the consecutive thermal annealing treatments.

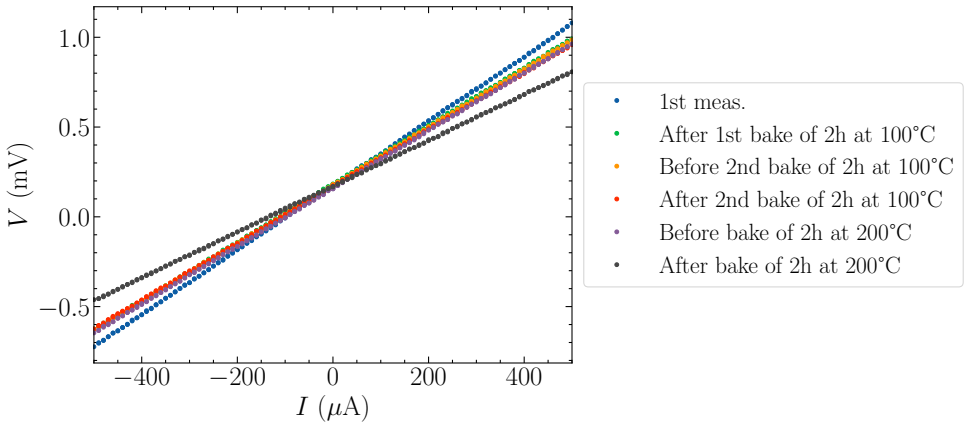

Figure 45: $I - V$ curves of the 3rd grAl sample of $t = 100$ nm during the consecutive thermal annealing treatments.

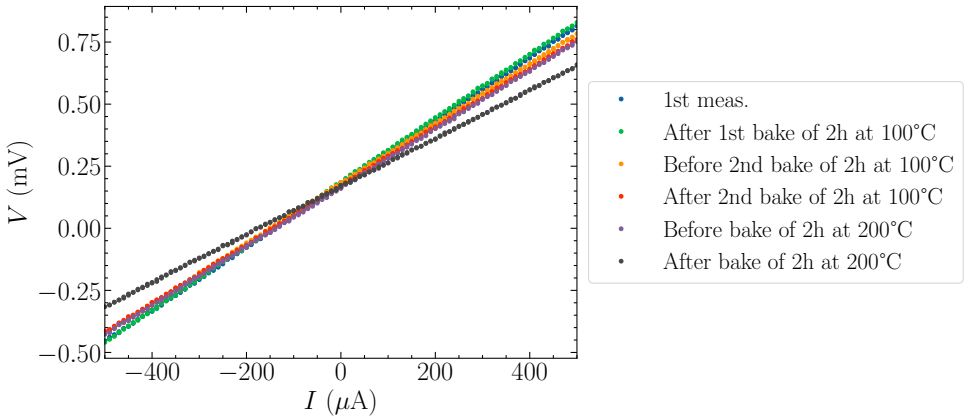

Figure 46: $I - V$ curves of the 3rd grAl sample of $t = 100$ nm, rotated by 90°, during the consecutive thermal annealing treatments.

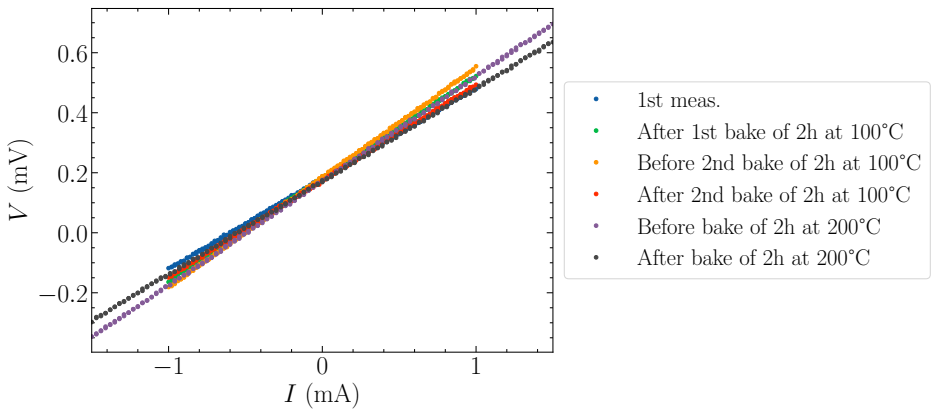

Figure 47: $I - V$ curves of the Al sample of $t = 25$ nm during the consecutive thermal annealing treatments.

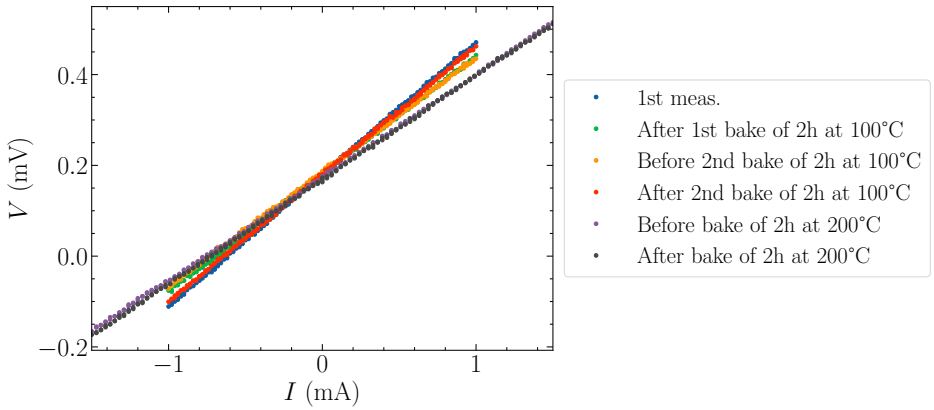

Figure 48: $I - V$ curves of the Al sample of $t = 25$ nm, rotated by 90°, during the consecutive thermal annealing treatments.

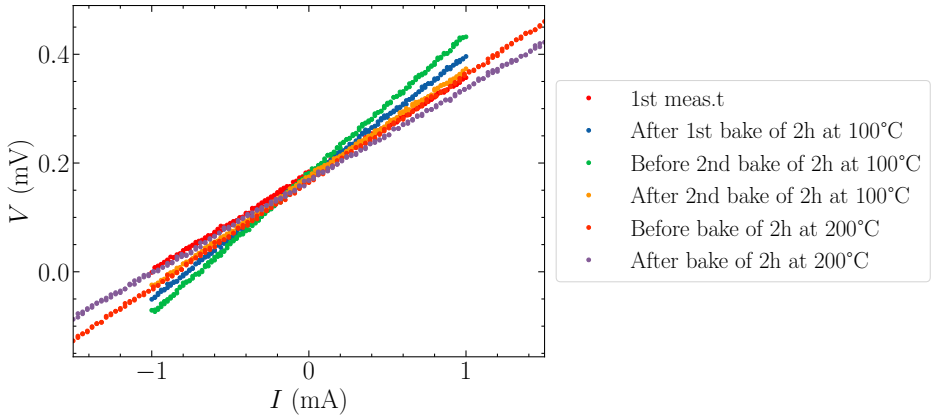

Figure 49: $I - V$ curves of the Al sample of $t = 50$ nm during the consecutive thermal annealing treatments.

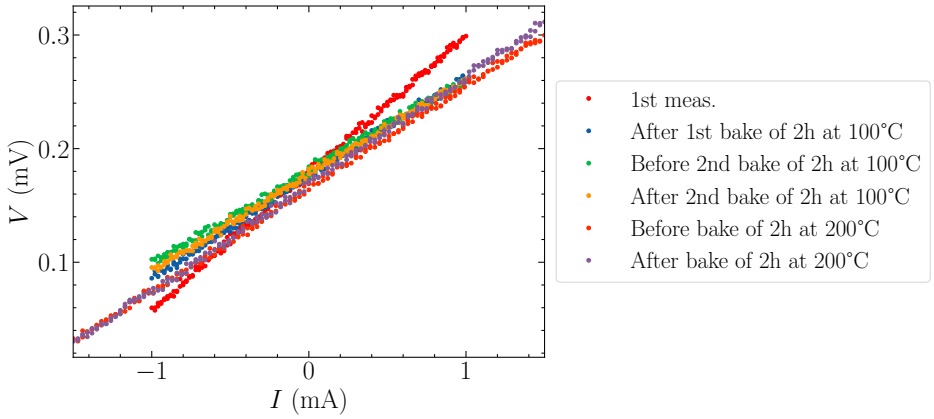

Figure 50: $I - V$ curves of the Al sample of $t = 50$ nm, rotated by 90°, during the consecutive thermal annealing treatments.

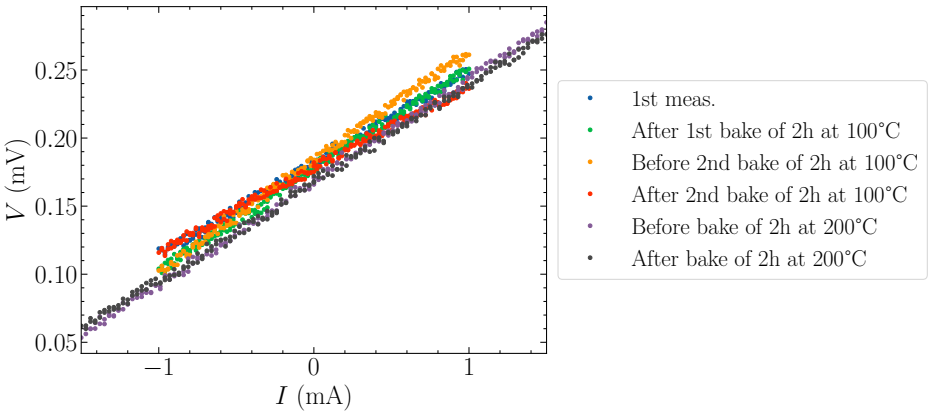

Figure 51: $I - V$ curves of the Al sample of $t = 100$ nm during the consecutive thermal annealing treatments.

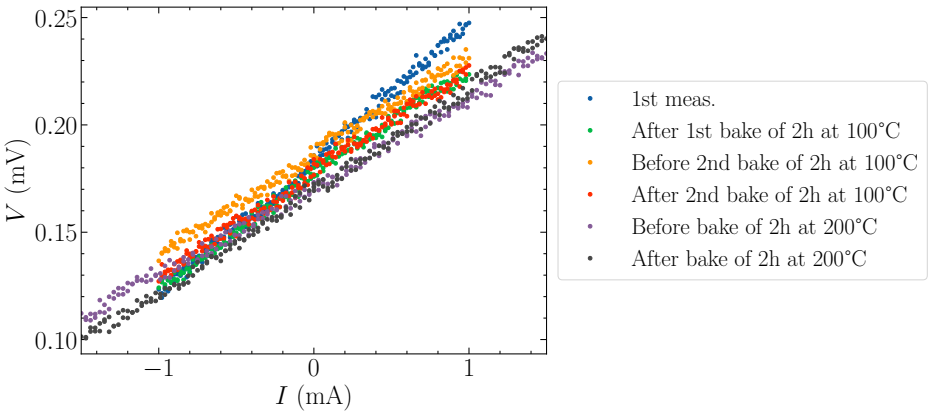

Figure 52: $I - V$ curves of the Al sample of $t = 100$ nm, rotated by 90°, during the consecutive thermal annealing treatments.

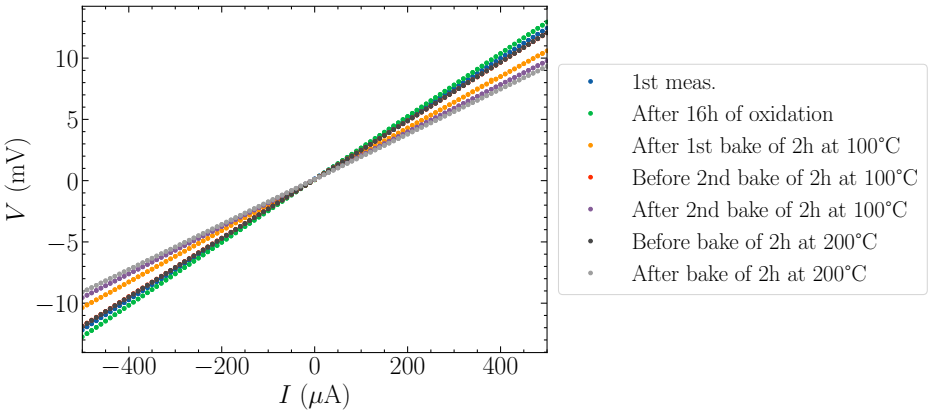

Figure 53: $I - V$ curves of the 1st NitrAl sample sputtered with a 13.3% N_2/Ar gas flow ratio of $t = 100$ nm during the consecutive oxidation and thermal annealing treatments.

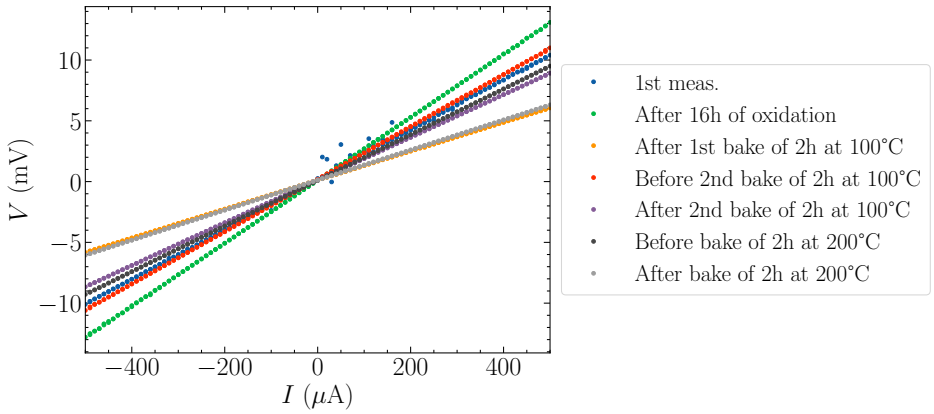

Figure 54: $I - V$ curves of the 2nd NitrAl sample sputtered with a 13.3% N_2/Ar gas flow ratio of $t = 100$ nm during the consecutive oxidation and thermal annealing treatments.

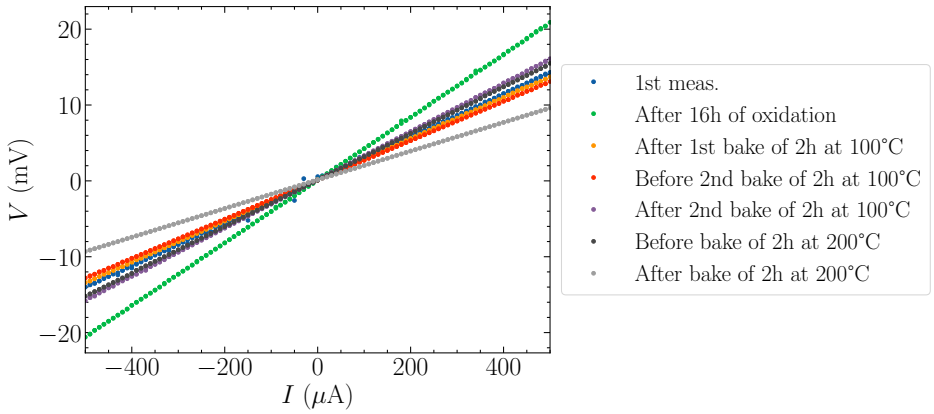

Figure 55: $I - V$ curves of the 3rd NitrAl sample sputtered with a 13.3% N_2/Ar gas flow ratio of $t = 100$ nm during the consecutive oxidation and thermal annealing treatments.

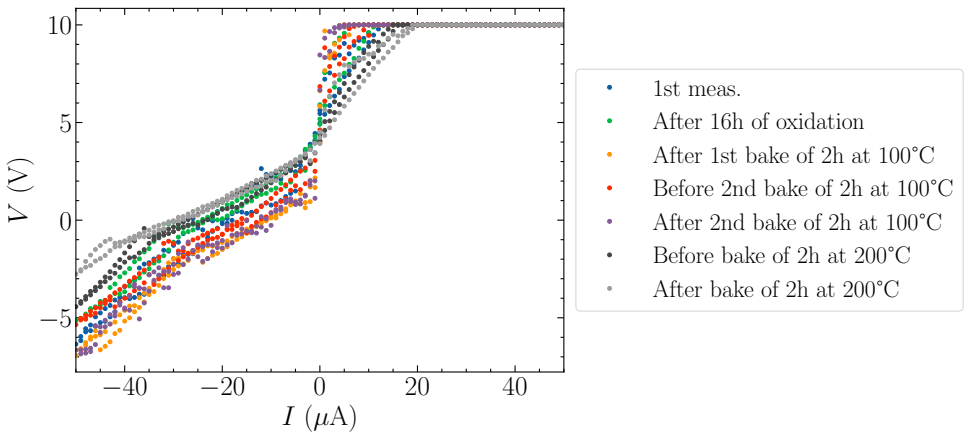

Figure 56: $I - V$ curves of the NitrAl sample sputtered with a 15% N_2/Ar gas flow ratio of $t = 100$ nm during the consecutive oxidation and thermal annealing treatments.

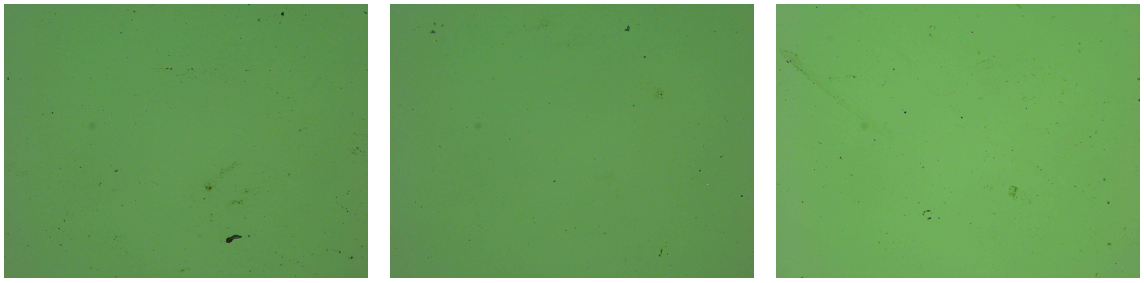

(a) **(b)** **(c)**

Figure 57: 20x augmented optical images of 1st run sample with resist sputtered with a 15% Ar/N_2 gas flow ratio. **(a)** Before bakes. **(b)** After a 2-hour long bake at 100°C. **(c)** After a 2-hour long bake at 200°C.

An interesting commentary about $I - V$ curves is that dispersion in them is a characteristic trait of insulators, which do not have a well-defined resistance. For instance, Figures 47 to 52 show that, for smaller thickness, the resistance curves are more disperse. This is in alignment with the fact that, for pure Al, with decreasing thickness resistance and resistivity are higher. Furthermore, Figure 56 exhibits the full insulator behaviour of the NitrAl 15% N_2/Ar gas flow ratio thin film. This is reflected in how far the curves are from a linear dependence, with a sizeable dispersion, and in the large range of voltage that is measured from the currents.

H Resonator fitting methodology

The fitting of the resonators studied in this work was done following the standard procedure described in [P+15, Gao08], from an adaptation of a code from KIT [kit]. Additionally, the iminuit [imi] Python library is employed, amongst others, to better address error propagation.

The core of the fitting model relies on the fact that the complex S_{21} transmission parameter of a notch-type resonator can be modelled as

$$S_{21}^{\text{notch}}(f) = a \cdot e^{i\alpha} \cdot e^{-2\pi i f \tau} \left[1 - \frac{(Q_L/|Q_e|)\, e^{i\phi}}{1 + 2iQ_L(f/f_0 - 1)}\right], \tag{10}$$

where:

- a is the amplitude, which comes from the attenuation and gain in the measurement system.
- α is the initial phase shift.
- τ is the electronic or cable delay. It originates in the finite nature of the length of circuitry cables and the speed of light.
- Q_L, as mentioned before, is the loaded or total quality factor.
- Q_e, as also explained before, is the external quality factor, which reflects losses in resonators due to external circuitry and reflects the coupling to them. For our purposes, it is modelled as a complex variable,

  $$Q_e = |Q_e|e^{-i\phi},$$

  where ϕ accounts for impedance mismatches. Due to being complex, in all the graphical representations of this work, Q_e has been considered to correspond to $|Q_e|$.
- Q_0 is the internal quality factor, which, as aforementioned, accounts for the intrinsic losses of the resonators.
- f_0, as usual, corresponds to the resonant frequency of the resonator.

Note that, out of all seven parameters to fit, a, α and τ are related to the environment of the resonator and its losses.

The first part in the obtaining of the resonant frequency and quality factors from the raw S_{21} resonator data consists on a "circle fitting" method. This procedure starts by fitting the cable delay, τ. This can be ascertained from the graphical representation of $\text{Im}(S_{21})$ vs. $\text{Re}(S_{21})$. Ideally, in the absence of delay, that graphic should be a perfect circle of center $z_c = (x_c,\ y_c)$ and radius r_0. Nonetheless, τ introduces some distortion to it in the form of a curve loop. After a first rough estimate, τ is determined by means of the `least_squares` SciPy function, which minimizes the deviation of the shape from a perfect circle. Then, the data is corrected according to the obtained value.

Once the cable delay has been calculated, x_c, y_c and r_0 must be determined. To do so, an initial guess of the coordinates of the center is estimated as the arithmetic mean of the data points. That first guess serves as an input for the `leastsq` SciPy function to compute the actual coordinates by minimizing the algebraic distance between the points and the ideal circle. The radius is then computed as the arithmetic mean of the distances

of the points to the center of the circle. The error in this fitting is calculated as the square root of the diagonal elements of the product between the inverse Hessian matrix and the residual variance, obtained as outputs of the fittings.

At this point, the modified S_{21} data looks like a circle in the complex plane displaced by an affine transformation given by the center of the circle. Hence, a translation to the origin of the plane is needed. This translation is applied as

$$z_i = z_{i,0} - z_c,$$

where z_i are the raw S_{21} data points.

The succeeding step is to obtain the resonant frequency f_0, the loaded quality factor Q_L and the offset initial phase θ_0. For this purpose, a phase vs. frequency representation of the previously modified S_{21} data is needed. This dependence can be modelled as

$$\theta(f) = \theta_0 + 2\arctan\left[2Q_L\left(1 - \frac{f}{f_0}\right)\right].$$

An iterative fitting method, which involves the usage of the `curve_fit` SciPy function, is performed with the aim of obtaining our three parameters of interest.

Following that, a translation of the data, now in the real plane, is executed. To start with, the angular position of the off-resonant point, P is computed. That point is the coordinates of the circle that correspond to $f = \infty$, and should ideally be placed at $P = (1, 0)$. In practice, however, P is rotated by an angle β. This angle is obtained as

$$\beta = (\theta_0 + \pi) \mod 2\pi,$$

thus imposing $\beta \in [0, 2\pi]$.

Once β is attained, the off-resonant point is calculated as

$$P = x_c + r_0\cos(\beta) + i\left[y_c + r_0\sin(\beta)\right].$$

Note that this point is a complex coordinate. From this, the initial phase shift and the amplitude are extracted as

$$\alpha = \arg(P), \quad a = \mathrm{Re}(P).$$

Lastly, the S_{21} data points are rotated and translated. To do so, they are multiplied by $e^{2\pi i f\tau}$, which corrects the cable delay, and by $e^{-i\alpha}$ to correct the initial phase shift. Additionally, they data is normalized by the factor a.

After this last data adjustment, r_0 and z_c are corrected and, from those, the remaining fit parameters are computed. First, the impedance mismatch is computed as

$$\phi = -\arcsin\left(\frac{y_c}{r_0}\right).$$

After that, the external quality factor is calculated as

$$Q_e = \frac{Q_L}{2r_0 e^{-i\phi}},$$

and, lastly, from that latest variable the internal quality factor is obtained as

$$\frac{1}{Q_0} = \frac{1}{Q_L} - \mathrm{Re}\left(\frac{1}{Q_e}\right).$$

After the first parameter fitting of the resonator, final adjustments and corrections are additionally performed by means of the iminuit library to refine the fitting of Equation 10.

Figures 58 and 59 exemplify the previous method for resonator fitting applied to the simulated resonators of the photolithographic mask design. The first step, regarding the calculation of the cable delay, is not included, since these images pertain to simulated data, and therefore losses due to the environment are nonexistent. These are better represented in Figure 60, which depicts the fitting of an experimentally measured resonator.

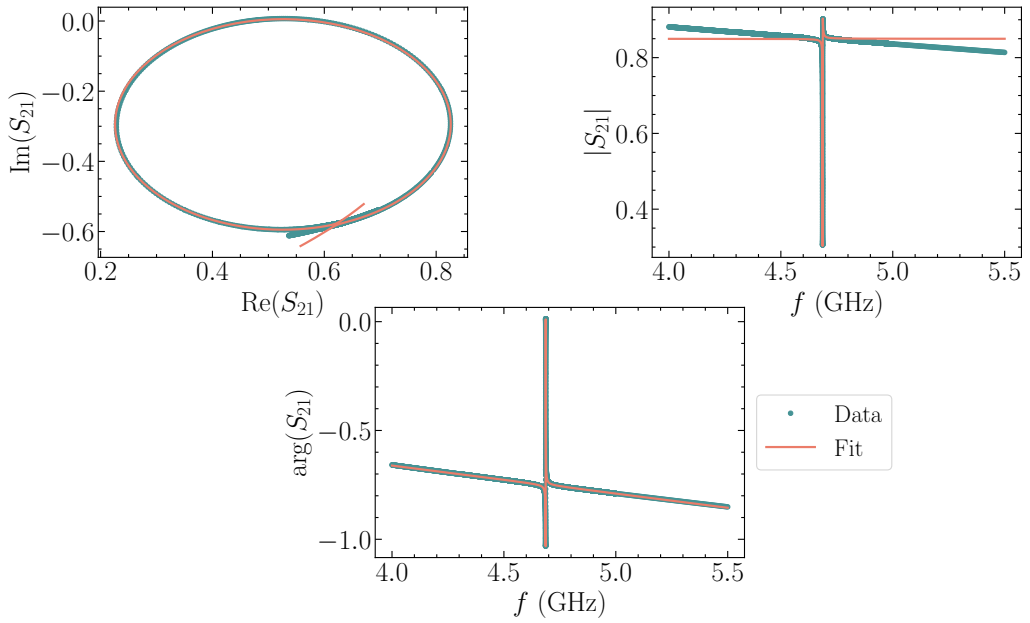

Figure 58: Figures related to the fitting procedure of the longest resonator (resonator 1) in the photolithographic mask design.

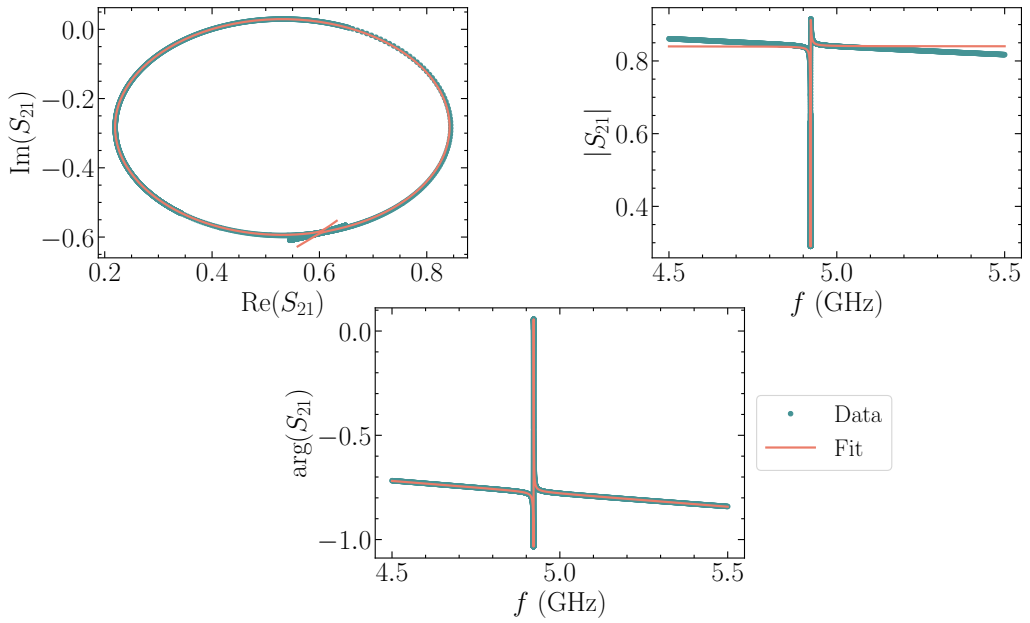

Figure 59: Figures related to the fitting procedure of the shortest resonator (resonator 5) in the photolithographic mask design.

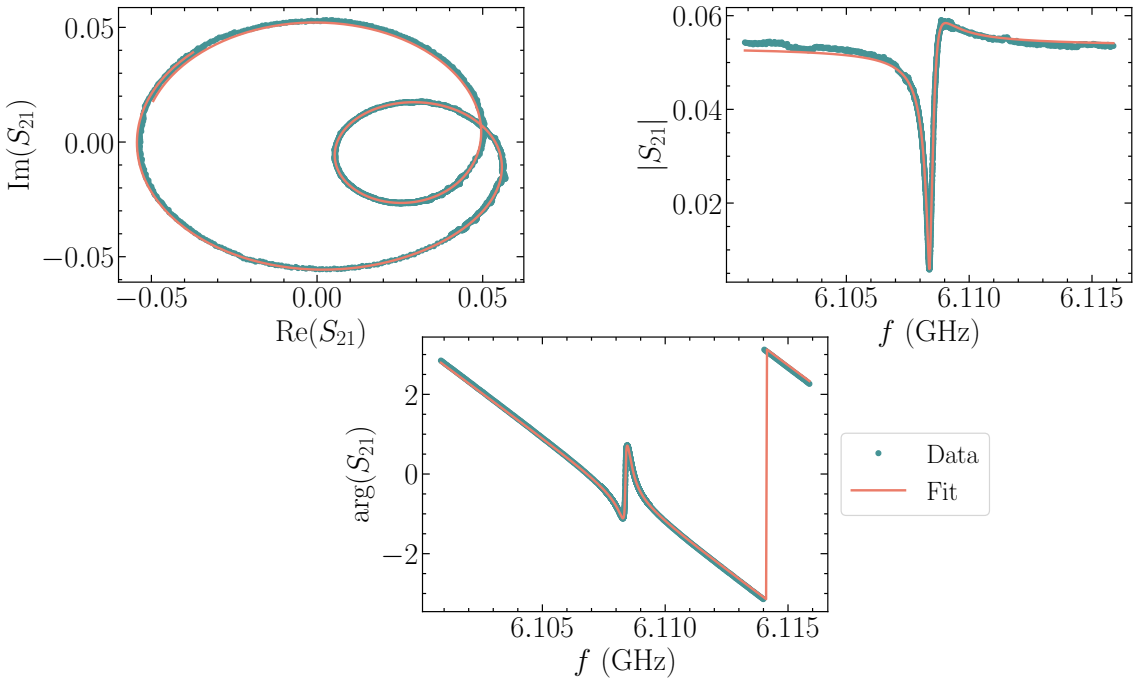

Figure 60: Figures related to the fitting procedure of the measured resonator 1 at $T = 27$ mK.

I Geometry and materials of resonators and behaviour at resonance

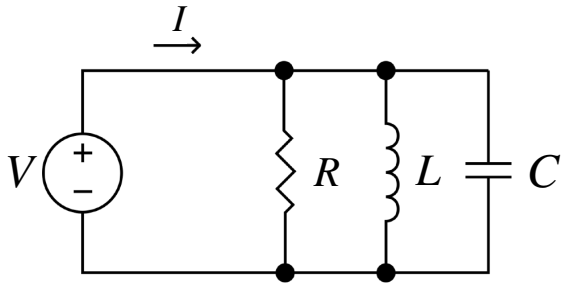

Figure 61: Parallel RLC lumped-element resonator.

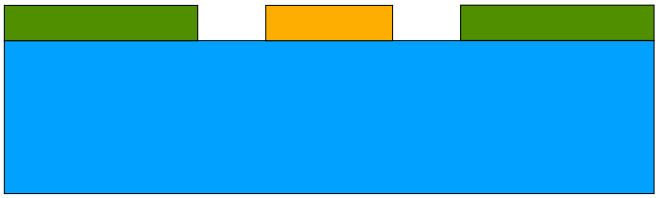

Figure 62: Schematic representation of the cross section of a CPW transmission line. The insulating substrate is coloured in blue, the conducting ground planes are represented in green and the conducting line through which current is transmitted is presented in yellow. The ground planes and central line are fabricated with the same material.

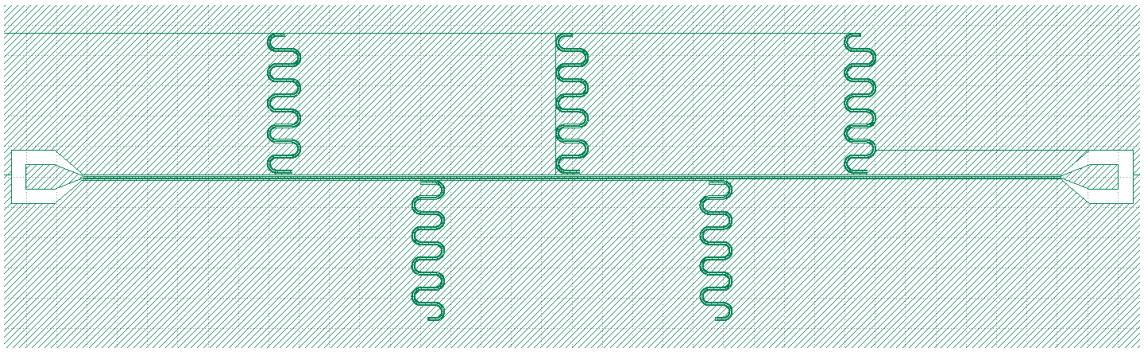

Figure 63: Distribution of the resonators in the design of the photolithographic mask developed for the study of NitrAl, containing five $\lambda/4$ CPW resonators inductively coupled to feedline. The differences in lengths are added in the straight paths between meanders. The distance between resonators was set so that they did not influence each other (i. e., to avoid cross-talking).

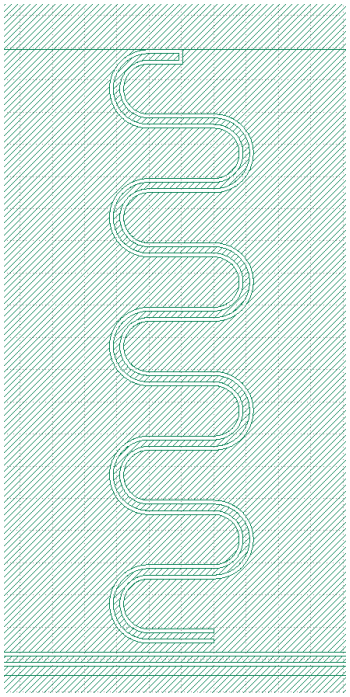

Figure 64: Zoom-in of one of the resonators in Figure 63 and its coupling to the feedline. For all cases, the width of the resonators' central transmission line and the feedline was set to be 10 μm, and the distance from the central transmission lines to the ground planes is 6 μm.

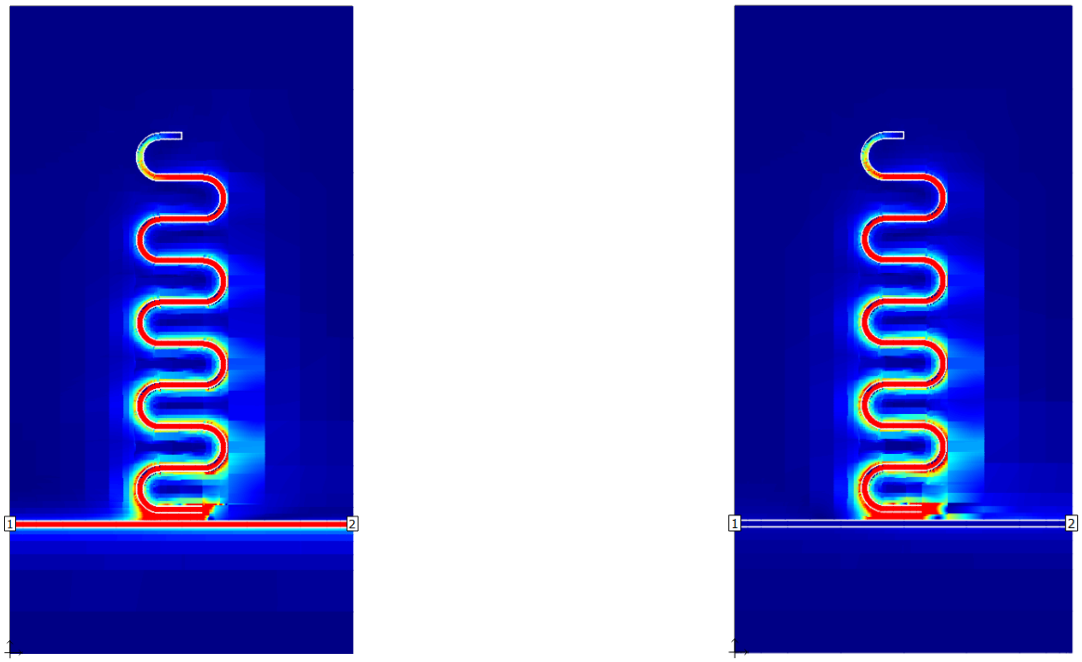

(a) (b)

Figure 65: Simulated current distributions at resonance of the shortest and longest resonators in the photolithographic mask designed for this project. As expected, for the resonant frequency of the fundamental mode only a quarter of a wavelength travels through the resonator, with a current maximum in the short-circuited end and a current minimum in the open-circuited end.

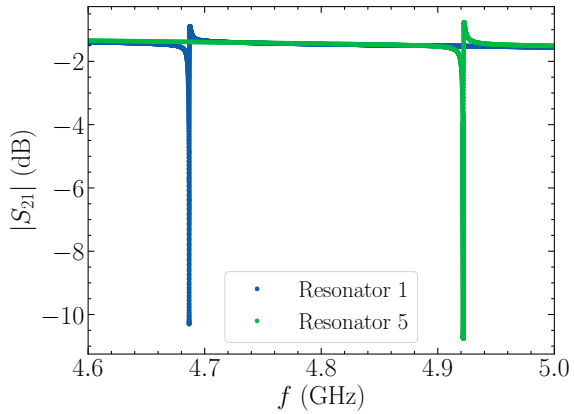

Figure 66: $|S_{21}|$ parameter as a function of frequency in the vicinity of f_0 of the resonators of lower and highest resonant frequencies in the photolithographic mask design.

The design of the geometry of the resonators was crafted via the `gdspy` Python library [gds]. The resulting individual GDSII files, which included the feedline, the separate resonators and the ground of the CPW up to a distance of 300 μm of the resonator as well, were entered into Sonnet for the forthcoming simulation.

The materials input in the simulations were selected from the available material library in Sonnet and modified to better resemble our particular conditions.

- For the substrate, insulating Si was emulated by a relative permittivity of $\varepsilon_{\text{rel}} = 11.45$, a dielectric loss tangent of $\tan(\delta) = 5 \cdot 10^{-5}$, null conductivity, a relative permeability of $\mu_{\text{rel}} = 1$ and a magnetic loss tangent of $\tan(\delta_\mu) = 0$. Its thickness was set to be 500 μm, a standard value for chip substrates.

- Superconducting NitrAl was imitated by a modified Al planar metal layer. The "General" model was selected, which is appropriate for systems of infinitesimal height that can be approximated as a 2D sheet. In this case, DC sheet resistance, RF sheet resistance and DC reactance were $R_{\text{dc}} = R_{\text{rf}} = X_{\text{dc}} = 0$ to simulate superconductivity. Additionally, the thickness was set to be 100 nm, the standard in the 1st run samples. The sheet inductance was accounted as $L_\square = 23.91$ pH/$\square$. This was input because it was one of the highest estimated kinetic inductance values in [TC+24] for samples that still experienced a metal-to-superconductor transition. Since $\omega_0 \sim 1/\sqrt{L}$, a higher kinetic inductance implies a lower resonant frequency. By simulating resonators that have one of the lowest resonant frequencies, we ensure that the frequencies will still be measurable in the scenario that the high estimated kinetic inductance values are not reproducible or that external losses that cannot be accounted for in simulations negatively affect the experimental realisation of the resonators, increasing ω_0.

- To mimic air as the top material of the sample, $\varepsilon_{\text{rel}} = \mu_{\text{rel}} = 1$ and $\sigma = \tan(\delta) = \tan(\delta_\mu) = 0$ were set, with a thickness of 5000 μm.

An interesting observation from Figure 66, which is also present in Figure 60, is the fact that the resonance dips are not symmetric before and after f_0. The cause of this anomaly is known to be impedance mismatch; that is, the input impedance of the central transmission line that conforms the resonator not being $Z_0 = 50\ \Omega$. This disadvantage imposes difficulty in detecting resonance dips when measuring resonators. The devices

in the photolithographic mask, nonetheless, were thoughtfully designed to meet that requirement, and it was checked with input impedance calculations, which gave rise of values $Z_0 \sim 49.2\ \Omega$. This, however, seems to not have been enough precision in order to avoid impedance mismatch.

J Δf_0 and quality factors of resonators

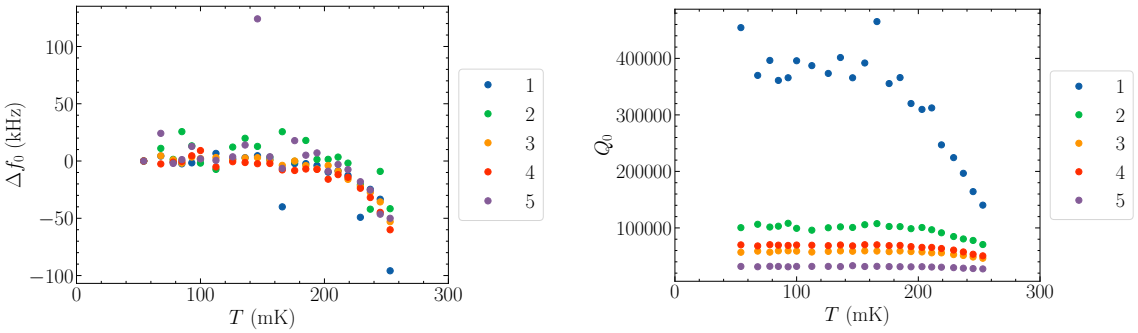

(a) **(b)**

Figure 67: Shift in f_0 and Q_0 of Al resonators as a function of temperature. **(a)** Δf_0. **(b)** Q_0.

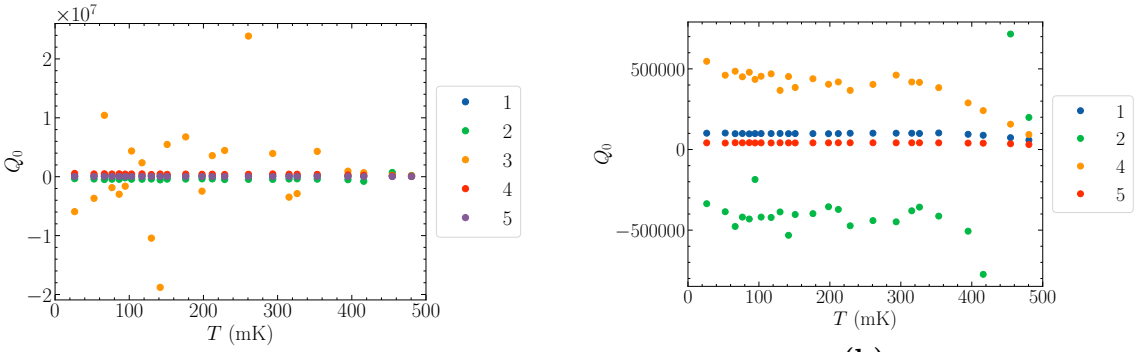

(a) **(b)**

Figure 68: Q_0 of the measured NitrAl resonators as a function of temperature. **(a)** All resonators. **(b)** Zoom-in.

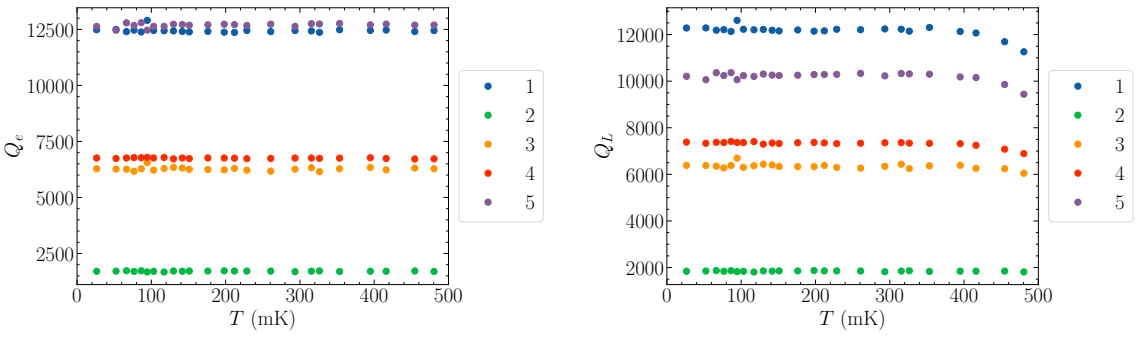

(a) **(b)**

Figure 69: Quality factors of the measured NitrAl resonators as a function of temperature. **(a)** Q_e. **(b)** Q_L.

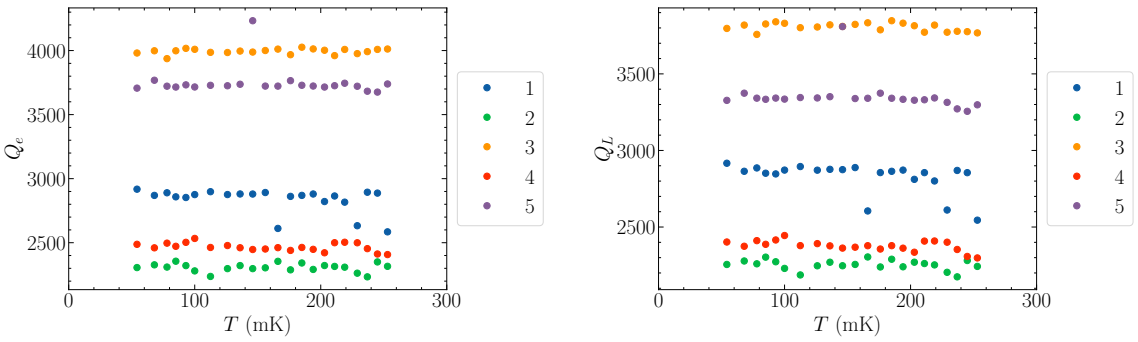

(a) **(b)**

Figure 70: Quality factors of the measured Al resonators as a function of temperature. **(a)** Q_e. **(b)** Q_L.